

Fall 12-13-2013

Enhanced Sonar Array Target Localization Using Time-Frequency Interference Phenomena

Jordan Almon Shibley
Portland State University

Follow this and additional works at: https://pdxscholar.library.pdx.edu/open_access_etds



Part of the [Signal Processing Commons](#)

Let us know how access to this document benefits you.

Recommended Citation

Shibley, Jordan Almon, "Enhanced Sonar Array Target Localization Using Time-Frequency Interference Phenomena" (2013). *Dissertations and Theses*. Paper 1488.
<https://doi.org/10.15760/etd.1487>

This Thesis is brought to you for free and open access. It has been accepted for inclusion in Dissertations and Theses by an authorized administrator of PDXScholar. Please contact us if we can make this document more accessible: pdxscholar@pdx.edu.

Enhanced Sonar Array Target Localization
Using Time-Frequency Interference Phenomena

by

Jordan Almon Shibley

A thesis submitted in partial fulfillment of the
requirements for the degree of

Master of Science
in
Electrical and Computer Engineering

Thesis Committee:
Lisa M. Zurk, Chair
Martin Siderius
Daniel Rouseff

Portland State University
2013

Abstract

The ability of traditional active sonar processing methods to detect targets is often limited by clutter and reverberation from ocean environments. Similarly, multipath arrivals from radiating sources such as ships and submarines are received at sensors in passive sonar systems. Reverberation and multipath signals introduce constructive and destructive interference patterns in received spectrograms in both active and passive sonar applications that vary with target range and frequency. The characterization and use of interference phenomena can provide insights into environmental parameters and target movement in conjunction with standard processing methods including spectrograms and array beamforming.

This thesis focuses on utilizing the time-frequency interference structure of moving targets captured on sonar arrays to enhance the resolution and abilities of conventional sonar methods to detect and localize targets. Physics-based methods for interference-based beamforming and target depth separation are presented with application of these methods shown using broadband simulated array data.

Acknowledgments

I would like to thank my thesis adviser Dr. Lisa Zurk for all of her help and support through my studies and research. I also wish to thank Dr. Martin Siderius and Dr. Daniel Rouseff for their input and for serving on my thesis committee. To all of my peers in the NEAR-Lab, I would like to extend my gratitude for the discussion and conversations we have had. Finally, I would like to thank the Office of Naval Research for funding this research.

Contents

Abstract	i
Acknowledgments	ii
List of Tables	vi
List of Figures	vii
1 Introduction	1
1.1 Executive Summary	1
1.2 Thesis Contributions	4
2 Acoustic Propagation	6
2.1 Shallow Water Propagation	7
2.1.1 Ray Propagation	7
2.1.2 Shallow Water Sound Speed Profile	9
2.2 Deep Ocean Propagation	12
2.2.1 Deep Water Sound Speed Profile	12
2.2.2 Reliable Acoustic Path	14

2.2.3	Deep Ocean Noise	18
2.3	Normal Mode Model	21
3	Waveguide Invariance	25
3.1	The Passive Invariant	25
3.2	The Active Invariant	28
4	Array Processing	30
4.1	Array Geometry	30
4.2	Conventional Beamforming	31
4.3	Invariance Striation Beamforming	34
5	Simulation and Analysis	37
5.1	Automatic Striation Extraction	37
5.2	Horizontal Line Array	43
5.3	Deep Vertical Line Array	48
6	Depth Based Signal Separation	55
6.1	Depth Based Signal Separation	56
6.2	Simulated Harmonic Transform Results	60
7	Summary and Future Work	67
7.1	Summary	67
7.2	Future Work	69

List of Tables

5.1	Detected striations in deep VLA simulation using the striation extraction method outlined in Section 5.1 and result presented in Figure 5.6. Slope is given as Δf , described in equation 4.3.	51
6.1	Deep VLA simulation parameters for depth-based signal separation transform.	60
6.2	Calculated unambiguous depth limits based on VTR tracks from Figure 6.4 using equation 6.5.	65

List of Figures

2.1	Reflection and transmission at interface between two media. Adapted from Computational Ocean Acoustics [14].	9
2.2	Shallow water sound speed profiles adapted from Kuperman [18]. (a) Fully mixed winter isovelocity sound speed causing minimal refraction within the water column. (b) 3-Layer summer profile consisting of the surface mixed layer with increased sound speed from seasonal warming above a thermocline reducing sound speed with increased depth to the bottom mixed layer.	11
2.3	The deep ocean sound speed profile. (a) Characteristic deep ocean sound speed profile adapted from Kinsler [15] showing regions increasing in depth: surface layer, seasonal thermocline, main thermocline, and deep isothermal layer. The deep sound channel axis marks the minimum sound speed. The critical depth marks the depth at which the sound speed exceeds the maximum present near the ocean surface. (b) Idealized Munk sound speed profile for 5 <i>km</i> water depth [14, 19].	13

2.4	Deep ocean ray plots showing reliable propagation paths <i>i.e.</i> paths without bottom or surface interaction. Ray paths calculated using the Ocean Acoustics Toolbox BELLHOP program [10] with the Munk sound speed profile from Figure 2.3b. (a) Source at 200 <i>m</i> depth with propagation exhibiting convergence zones appearing at 60 <i>km</i> intervals. (b) Source at 1.3 <i>km</i> depth showing long range propagation around the deep sound channel axis. (c) Source at 4.5 <i>km</i> depth depicting the spatial separation of rays propagating to the surface at various ranges based on the transmit angle from the source location. Additional red ray traces indicate paths at close ranges with surface incidence showing reliable path to surface targets.	16
2.5	Deep ocean TL simulation created using the Ocean Acoustics Toolbox KRAKEN program [17] with the Munk sound speed profile from Figure 2.3b. Solutions computed using source frequency of 150 <i>Hz</i> . (a) TL plot for 100 <i>m</i> source propagating to 35 <i>km</i> showing RAP to deep ocean bottom. (b) TL plot for 100 <i>m</i> source propagating to 150 <i>km</i> range showing convergence zones from deep sound channel refraction.	18
2.6	Characteristic deep ocean ambient noise spectrum adapted from Kinsler [15]. Ambient noise levels show possible ranges from shipping traffic and sea state. Wind speeds are indicated in knots (<i>kts</i>).	19

2.7	Deep ocean noise plots adapted from Gaul <i>et al.</i> [11]. (a) Wind noise measured below critical depth at 50 Hz . (b) Wind noise measured below critical depth at 300 Hz . (c) Simulated distant shipping noise at 50 Hz for surface ships at variable range.	22
3.1	Acoustic data recorded by the NEAR-Lab on the Columbia River, OR, of a small boat traveling past a single hydrophone. (a) Spectrogram of acoustic data exhibiting invariance striations changing in slope and spacing with source range. (b) Small boat range to receiver showing symmetrical curvature similar to spectrogram striations.	27
4.1	Diagram showing array placement for towed horizontal line array (HLA) and deep vertical line array (VLA).	31
4.2	Diagram of delay between array elements of an incident plane wave with inter-element spacing d , incident angle ϕ , and N total array elements. $x_{n-1}(t)$ represents the recorded acoustic data for the n th of N total array elements.	32

5.1	Radon projection example illustrating localized peaks associated with sloped lines. (a) Test image containing two lines with 135° projected slopes and one with a 45° slope. (b) Radon transformed test image from (a) showing peaks corresponding to the slopes of the lines present. The two parallel lines with 135° projected slope occur at the same projection angle with radial distance from the origin of the test image preserved.	40
5.2	Striation slope extraction with Radon transform and Fourier decomposition. (a) Spectrogram of simulated snapshot received on hydrophone array. Invariance striations are visible in body of spectrogram. (b) Radon transformation of the phone-frequency spectrogram over a selected range of radial angles with a scaled slope given as change in frequency Δf over the array. (c) Fourier decomposition of each projected slope yields a peak corresponding to the slope and spacing of the striations from the array spectrogram. Spacing axis is scaled for 0° projection angle.	43

5.3	Simulated broadband beamformer plots shown with 40 <i>dB</i> dynamic range referenced to the maximum output. (a) Conventional beamformer output giving target bearing at 160°. (b) Striation-based conventional beamformer without phase-compensation term indicating target presence near 180°. (c) Striation-based conventional beamformer with phase-compensation showing a corrected target bearing and preserving striation pattern within beamformer output.	45
5.4	Cuts through the beamformer maximums showing preserved striation pattern. (a) Comparison between conventional and striation-based conventional beamformer outputs. Striation-based (red) preserves striation pattern over the full bandwidth compared with the smoothed output of the conventional single-frequency result. (b) Cuts through striation-based beamformer outputs with target simulated moving at 160° bearing from 23 <i>km</i> to 23.1 <i>km</i> in 3 <i>m</i> increments.	47
5.5	Deep VLA single hydrophone spectrogram simulated with Munk profile shown in Figure 2.3b. (a) Source-receiver geometric direct path range for 100 <i>m</i> source moving at a constant 5 <i>m/s</i> velocity and 4950 <i>m</i> receiver depth. (b) Single phone spectrogram limited to the simulated frequency band.	49

5.6	Striation slope extraction with Radon transform and Fourier decomposition. (a) Spectrogram of simulated snapshot received on hydrophone array. Invariance striations are visible in body of spectrogram. (b) Radon transformation of the phone-frequency spectrogram over a selected range of radial angles with a scaled slope given as change in frequency Δf over the array. (c) Fourier decomposition of each projected slope yields a peak corresponding to the slope and spacing of the striations from the array spectrogram. Spacing axis is scaled for 0° projection angle. (d) Fourier decomposition of each projected slope with local maxima marked. Associated slopes and spacing for the marked (color-coded) striation detections are recorded in Table 5.1.	50
5.7	Spectrogram from Figure 5.6a including extracted slopes from Table 5.1 indicated as overlays.	51
5.8	Vertical time record plots shown with 40 <i>dB</i> dynamic range for simulated VLA data. (a) Conventional beamformer output giving target $\sin \theta = 0.3$. Multipath reflection from the bottom bounce is visible below the broadside axis. (b) Striation-based conventional beamformer without phase-compensation term. (c) Striation-based conventional beamformer with phase-compensation showing a corrected vertical angle and preserving striation pattern 6 from Table 5.1. (d) Cut through maximum beam comparing conventional and striation-based result. . .	54

6.1	Diagram of image theory geometry indicating separation of a submerged source and the image reflected over the surface boundary. Sources are separated in vertical angle θ based on range.	56
6.2	Depth based harmonic interference pattern from direct calculation of pressure through equation 6.1 followed by beamforming. Source is simulated moving on a constant speed trajectory, moving directly above a VLA at minute 90 of the 180 minute time span. (a) Simulated VTR for a source located 1 <i>m</i> below the surface showing low-frequency content in the $\sin \theta$ trajectory. (b) Simulated VTR for a source located 50 <i>m</i> below the surface exhibiting higher frequency content along the $\sin \theta$ trace. (c) VTR from (b) including spacing overlay indicating harmonic in $\sin \theta$	59
6.3	Diagram showing processing flow for depth-based signal separation as described by McCargar and Zurk [9].	61
6.4	Simulated deep VLA VTR and depth-based signal separation transform results. (a) VTR plot showing target tracks in $\sin \theta$. (b) VTR with overlaid traces used for depth-based signal separation transform. (c) Transform result for surface interferer using green trace from (b) indicating source at 10 <i>m</i> depth. (d) Transform result for submerged target using red trace from (b) indicating source at 75 <i>m</i> depth. . . .	63

Chapter 1

Introduction

1.1 Executive Summary

Sonar utilizes the propagation of acoustic waves to detect objects under water. Sonar systems are grouped into two categories: active and passive. Active sonar systems transmit a waveform and listen for echoes. An active system will generally transmit a known waveform, such as a pulse or a chirp, with specified frequency content and length, and then correlate received data with the transmitted signal. This is a process known as matched filtering and can provide gain for the desired signal without increasing the background noise. Passive systems only receive signals created by targets, such as ship or submarine engines, but can localize them using physics-based modeling methods to create an estimate of the source location from received data and knowledge of the environment.

In shallow water applications, precise knowledge of the environment is often limited, increasing the difficulty of passive source localization. In an active geometry, targets localized in range based on the time delay between transmitted and received signals. Acoustic waves in ocean environments are typically bounded by the surface and bottom comprising the ocean waveguide, thus creating multiple paths that signals can travel from a source point to a receiver point in the phenomenon known as

multipath propagation. From the multipath propagation of the transmitted waveform to and from the target, active sonar inherently increases the amount of clutter in received data. Scattering from the uneven seabed causes returns that can easily be mistaken for desired targets. Multipath reflections from all scattering surfaces will be received together, interfering constructively and destructively. Waveguide invariance is one approach to describing the interference phenomena caused by multipath propagation from a broadband signal source.

The waveguide invariant was introduced by Chuprov [1] and is obtained from normal mode theory with some simplifying assumptions about the environment. It is a scalar parameter used to characterize the interference caused by multipath propagation. The value of the scalar invariant shows limited variability with small changes in the specific properties of propagation such as bathymetry and sound speed, hence designation of the term “invariance”. In environments where these properties are not well known, the waveguide invariant can be a useful tool in helping identify and track moving acoustic targets. The interference from the multipath propagation can be observed in spectrograms that depict either the time-frequency or range-frequency structure of received signals. The constructive and destructive interference produces striations in these spectrograms that vary in slope as functions of range and frequency.

The invariant phenomenon was initially studied in relation to passive sonar applications in shallow water environments by Chuprov and his work was later popularized by Brekhovskikh and Lysanov [2]. More recently, the concept of waveguide invariance

has been extended to higher frequencies in active systems having both monostatic and bistatic geometries by the Northwest Electromagnetics and Acoustics Research Laboratory (NEAR-Lab) and others [3, 4, 5].

While the idea of the waveguide invariant was theoretically derived, experimental observations suggest a more variable behavior of the scalar and that it should therefore be modeled as a distribution [6]. Variation in the value of the waveguide invariant has motivated interest in being able to automatically estimate its value from receiver data in order to utilize the interference phenomenon without being constrained to an assumed scalar value. In environments exhibiting a strong dependence on variable sound speed within the water column, such as in the deep ocean, the invariant nature of this parameter has been shown to have a high sensitivity to both range and frequency.

In this thesis, a method involving image processing techniques is proposed and applied to simulated data in order to extract interference patterns. The method is applied to simulated invariance data in both shallow and deep water. Methods of striation slope extraction that are robust to additional interference and noise have also been the subject of recent study. The proposed image processing method is applied to one case in which the invariance phenomena is easily observable and to another where the phenomena presence is influenced by multipath interference. Using the results from the pattern extraction method, a physics-based beamforming method is applied to the simulated array data to preserve the invariance phenomenon in beamforming

as described by Zurk and Rouseff [7, 8].

Another interferenced based topic explored in this thesis is a passive, physics-based approach for estimating source depth. Passive multipath observed on a vertical line array placed on the ocean bottom (utilizing the reliable acoustic path geometry) has prompted research into the relation of source depth and spatial harmonic content of the multipath interference. Resolving targets in depth provides one of the strongest features for discriminating submerged targets from surface ships. However, the ability to localize targets within the water column has often been dependent on knowing exact environmental parameters such as locations of bathymetric features and sound speed. A physics-based processing method involving the depth-based harmonic interference structure of sources near the ocean surface presented in the work of McCarger and Zurk [9] is used to separate submerged targets from surface interferers. Parameters influencing the depth resolution of the proposed method are explored in extension of the original published work.

1.2 Thesis Contributions

This thesis makes the following contributions to previous work:

- Produced results from underwater acoustic propagation programs applied to horizontal and vertical line array geometries that exhibit interference striations associated with waveguide invariance.

- Demonstrated an enhanced method involving the Radon transform to automatically extract linear interference patterns from array data through the secondary processing of a Fourier transform. Successful implementation of proposed transform yields interference striation spacing in addition to the slope.
- Applied striation-based beamforming to simulated horizontal and vertical line array data preserving striation patterns in the beamformed output.
- Further characterized the depth separation technique by applying a resolvable depth limitation based on the time and spatial sampling of the depth-dependent harmonic.

Chapter 2

Acoustic Propagation

This chapter reviews the concepts associated with underwater acoustic propagation and the parameters that define the propagation space. This is used as a basis for the physics-based processing presented in later chapters of this thesis. This chapter is divided into two primary sections addressing the separate cases of shallow and deep water propagation. In the first section, Snell's law of refraction is used as a simple representation of the propagation of acoustic waves in an ocean waveguide bounded by the surface and seabed. The simplified case of a horizontally stratified, downward refracting, shallow water sound speed profile is described using refraction to demonstrate the sound speed dependence of plane wave propagation.

The Ocean Acoustics Toolbox BELLHOP program [10] ray tracing model is then applied to a characteristic deep ocean sound speed profile to describe the concept of the reliable acoustic path (RAP) in deep ocean propagation. A noise analysis of deep receiver location is then presented, including analysis from Gaul *et al.* [11] and Li *et al.* on deep ocean noise [12, 13].

The normal mode model is then presented as an alternative to the ray tracing model. The normal mode solution is used in subsequent chapters in the derivation of the scalar waveguide invariant and to compute pressure fields caused by a point source for range-independent environments.

2.1 Shallow Water Propagation

In shallow water environments, up to about 200 m , multipath propagation is introduced by the acoustic surface and bottom interaction comprising the shallow water waveguide. A simple representation of planar wave propagation is given in relation to wave boundary interaction through Snell's law.

The concept of variable sound speed within the water column is then presented with seasonal examples exhibiting variations with depth. Based on the variable sound speed, refraction within the water column is presented for shallow water, extending the idea of ray propagation with Snell's law.

2.1.1 Ray Propagation

The ocean waveguide boundaries are formed by the air-water interface and the ocean bottom. Incident acoustic energy reflects off of these boundaries (and potentially sub-sediment layers) back into the water column confining the propagation region. Incident waves on the air-water boundary can be considered perfectly reflected, meaning the entire wave is reflected back into the water column, due to the relative acoustic impedances of water and air. The lower boundary is often made up of layered sediments that have similar acoustic impedances to water. This causes part of the wave to be reflected back up into the water column, but a portion also penetrates and is transmitted into the sediment [14]. The interaction of the wave at the boundary is a function of the acoustic impedances of the two media defining the boundary.

The impedance of a given media is calculated from the density (ρ), sound speed (c), and the incident angle relative to the boundary (θ_i) using,

$$Z = \frac{\rho c}{\sin \theta_i}. \quad (2.1)$$

Snell's law of refraction states that the horizontal component of the incident wave vector must be preserved [14],

$$\frac{2\pi f}{c_1} \cos \theta_i = \frac{2\pi f}{c_1} \cos \theta_r = \frac{2\pi f}{c_2} \cos \theta_t, \quad (2.2)$$

where all grazing angles are shown in Figure 2.1 with the reflection and transmission between mediums 1 (top) and 2 (bottom). With conservation of the horizontal component of the wave vector, the relationship between the transmission coefficient T and reflection coefficient R can be written,

$$1 + R = T. \quad (2.3)$$

The reflection and transmission coefficients can be rewritten in terms of the effective impedances,

$$R = \frac{Z_2 - Z_1}{Z_2 + Z_1}, \text{ and } T = \frac{2Z_2}{Z_2 + Z_1}. \quad (2.4)$$

Examining Snell's law in equation 2.2, a transition from lower to higher sound speed

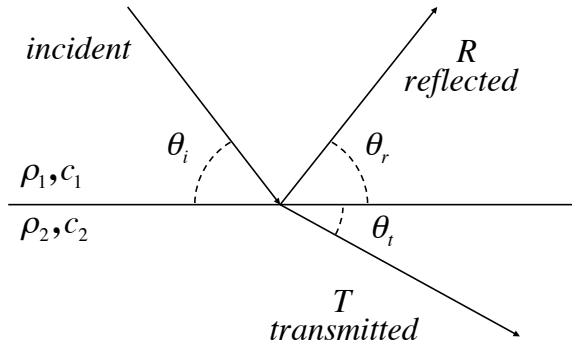


Figure 2.1: Reflection and transmission at interface between two media. Adapted from Computational Ocean Acoustics [14].

will cause the transmitted wave to refract towards the boundary. An important result from equation 2.4 is that when Z_1 and Z_2 are similar, meaning the layers are well matched, the majority of the wave is transmitted and reflection at the interface is limited.

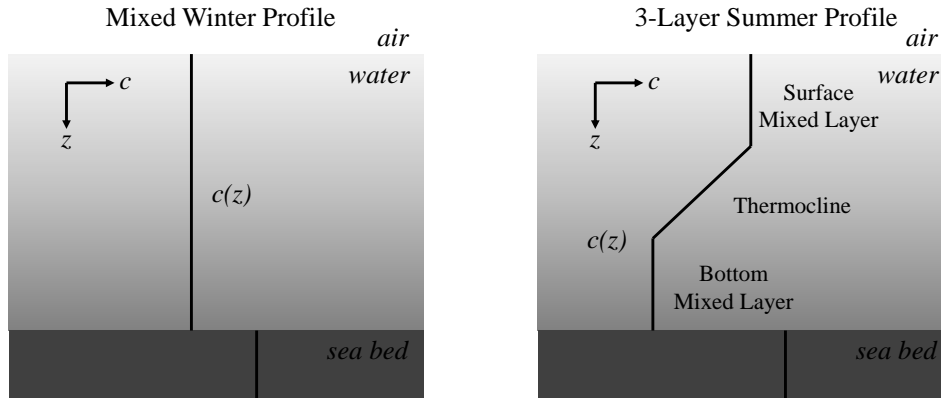
2.1.2 Shallow Water Sound Speed Profile

Extending the result for the single boundary example in Section 2.1.1, propagating through multiple layers with similar acoustic impedances causes waves to refract at each interface. As the layers become infinitely thin, a continuous gradient is approximated and a continually refracting ray can be calculated. This is an important result when considering the variability in sound speed within the ocean water column

and acoustic propagation over long ranges.

In shallow water, the sound speed profile is highly dependent on surface conditions. Seasonal heating causes the surface temperature to rise, creating a gradient from higher to lower sound speed as depth increases and temperature decreases. Similarly, cooling during colder months creates a more uniform sound speed profile by reducing the water temperature at the surface. Surface conditions add complexity to the profile in that the penetration of surface induced temperature changes can vary by the amount of mixing from the sea state. In addition, upwelling currents near coastal areas can cause mixing in deeper portions of the water column [16]. Due to the variability of the sound speed profile, it is often unknown and a nominal value must be selected when modeling the environment. An isovelocity assumption simplifies the propagation model by removing the refraction within the water column and reduces the ray-tracing methodology mentioned in Section 2.1.1 to boundary interactions and spreading loss. The isovelocity assumption is only applicable to very shallow or winter environments where the surface mixing extends to the sea floor. A comparison of the overall structure of a downward refraction profile compared with a fully mixed isovelocity profile is shown in Figure 2.2 [18].

While the relative acoustic impedances of the air-water interface are well defined, the waveguide bottom boundary is not easily accessible or consistent. As the bottom properties largely define the reflection and multipath propagation in an environment, it is important to characterize the density and sound speed of the seabed as well as the



(a)

(b)

Figure 2.2: Shallow water sound speed profiles adapted from Kuperman [18]. (a) Fully mixed winter isovelocity sound speed causing minimal refraction within the water column. (b) 3-Layer summer profile consisting of the surface mixed layer with increased sound speed from seasonal warming above a thermocline reducing sound speed with increased depth to the bottom mixed layer.

water column when defining a sound speed profile. Bottom composition can vary with geographic location as well as layering of different materials such as sediment, sand, and rock. Including a measured bottom composition and roughness in simulation will help account for bottom losses associated with multipath propagation, which has a dominant impact on long range transmission loss in shallow water environments [14].

For an environment with known parameters such as bottom composition, bathymetry, water depth, and sound speed profile, the acoustic waves from a source can be traced using Snell's law and a stratified approximation of the environment. From a point source, a ray with a defined takeoff angle can be traced through the stratified layers

by refraction of the ray at each consecutive layer transition. A comprehensive computational approach beyond the scope of this thesis is outlined in the Ocean Acoustics Toolbox BELLHOP documentation [10].

2.2 Deep Ocean Propagation

In the deep ocean, surface and bottom interactions have limited impact on long range acoustic propagation due to refraction within the water column. This section presents an idealized sound speed profile and acoustic refraction in the deep ocean. The concept of deep reliable acoustic path (RAP) for sources near the surface to deep receiver locations is presented with ray tracing models and transmission loss (TL) plots. Additionally, results from previous work [11, 12, 13, 15] are presented regarding noise in the deep ocean in support of the RAP phenomenon.

2.2.1 Deep Water Sound Speed Profile

Refraction from the variable sound speed profile can be a primary influence on the propagation of acoustic waves in the deep ocean. Localized factors such as pressure, temperature, and salinity cause spatial variations in the sound speed. The sound speed changes seasonally and with geographical location. Understanding the sound speed profile of the water column is what allows the tracing of wave refraction as acoustic signals propagate through the environment.

Sound speed increases with pressure, temperature, and salinity. Through the

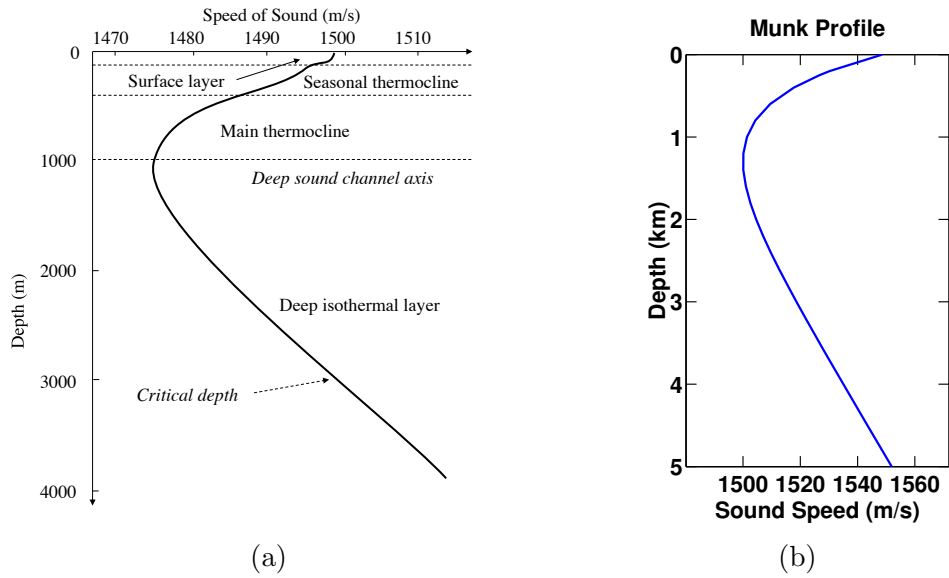


Figure 2.3: The deep ocean sound speed profile. (a) Characteristic deep ocean sound speed profile adapted from Kinsler [15] showing regions increasing in depth: surface layer, seasonal thermocline, main thermocline, and deep isothermal layer. The deep sound channel axis marks the minimum sound speed. The critical depth marks the depth at which the sound speed exceeds the maximum present near the ocean surface. (b) Idealized Munk sound speed profile for 5 km water depth [14, 19].

water column, each of these parameters has different regions where they are primary contributors. A typical deep water sound speed profile consists of four regions shown in Figure 2.3a [15]. The surface layer is highly subject to warming and cooling effects of surface conditions. Due to the fluctuation in temperature of daytime warming and nightly cooling, this layer can change frequently and is often unpredictable due to the mixing caused by the ocean state. These temperature and mixing effects can extend into the water column to approximately 200 m. Below this mixing layer, the effects of surface temperatures are less drastic, though the sound speed fluctuates with seasonal climate. With increasing depth, the temperature decreases consistently,

defining the main thermocline. The inflection point of the profile occurs at the deep sound channel axis. It is at this point that the temperature reaches a minimum and the deep isothermal layer begins. At constant temperature, the pressure increases consistently with depth causing the sound speed to increase. The critical depth is defined as the point in the deep isotherm where the sound speed reaches the maximum speed near the ocean surface. The Munk sound speed profile [14, 19] is an idealized sound speed profile that simplifies the profile near the surface. The Munk profile shown in Figure 2.3b is used for deep ocean simulations in subsequent chapters of this thesis with an acousto-elastic half-space consisting of a 100 *m* silt layer over a basalt basement.

2.2.2 Reliable Acoustic Path

Acoustic propagation in the deep ocean differs from the shallow water case due to the wave refraction from the sound speed profile. The deep sound channel is revealed by applying ray refraction to the characteristic deep ocean sound speed profile from Figure 2.3. Acoustic waves that enter the region between the maximum speed near the ocean surface and the critical depth will continually refract towards the deep sound channel axis as they propagate over range. Without any surface or bottom interaction, waves trapped in the deep sound channel will propagate long distances with minimal transmission loss.

The ray diagrams shown in Figure 2.4 were created with the Ocean Acoustics

Toolbox BELLHOP program [10] depicting selected ray paths for different source depths bending towards the deep sound channel axis. The sound speed used in ray calculation was the Munk profile included in Figure 2.3b. The ray diagram can be used to trace transmitted waves from a source to a range of receiver locations or incoming rays at a single receiver point due to reciprocity. With reciprocity of ray propagation, the traced paths also show the convergence of rays propagating from sources at locations in the waveguide, coinciding with the ray paths, to a single receiver point. The three ray plots in Figure 2.4 contain select transmitted paths from a source without boundary interactions. Figure 2.4a projects rays from a source at 200 *m* with convergence zones appearing every 60 *km* in range, where the refracted paths return to the surface after travelling nearly the full depth of the water column. Figure 2.4b places a source at the deep sound channel axis (1.3 *km* depth) and shows refracted paths covering a large portion of the water column and propagating to distant ranges. Figure 2.4c depicts the RAP from a 4.5 *km* deep source to the surface out to moderate surface ranges on the order of 40 *km* based on different transmission angles at the source point. In addition to rays without boundary interaction, rays to nearby surface ranges are shown in red. Dashed red lines show the unreliable multipath propagation of signals coinciding with trajectories to nearby surface targets. Through reciprocity, the solid red and blue rays indicate reliable signal propagation from near-surface targets out to moderate ranges without boundary interaction.

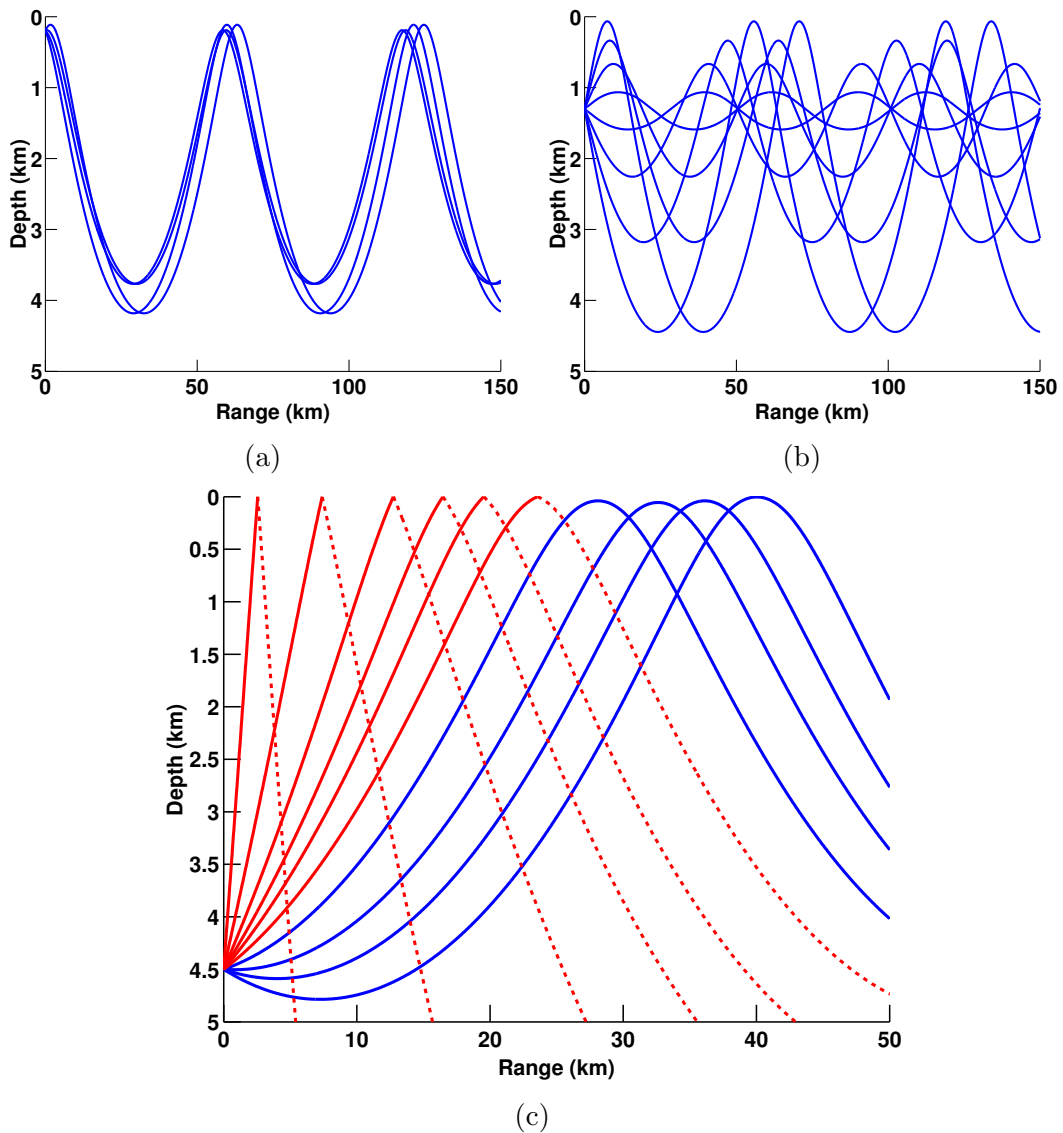


Figure 2.4: Deep ocean ray plots showing reliable propagation paths *i.e.* paths without bottom or surface interaction. Ray paths calculated using the Ocean Acoustics Toolbox BELLHOP program [10] with the Munk sound speed profile from Figure 2.3b. (a) Source at 200 *m* depth with propagation exhibiting convergence zones appearing at 60 *km* intervals. (b) Source at 1.3 *km* depth showing long range propagation around the deep sound channel axis. (c) Source at 4.5 *km* depth depicting the spatial separation of rays propagating to the surface at various ranges based on the transmit angle from the source location. Additional red ray traces indicate paths at close ranges with surface incidence showing reliable path to surface targets.

In passive sonar applications, receiver placement in deep oceans has a direct impact on the ability to locate targets based on the refracted paths as acoustic waves propagate through the environment. Limiting receiver placement to the top portion of the water column, the convergence zones shown in Figure 2.4a create an obstacle in locating targets in range. The areas between surface convergence zones are not reliably ensonified by shallow sources as the acoustic signals immediately refract downward as they are transmitted. Similarly, receivers placed near the deep sound channel axis do not have a reliable path to the surface and receive signals from long distances, ambiguous in range due to the same convergence zone effects from sources near the surface. Recent research has focused on utilizing the RAP geometry exploitable by deep receiver placement [9, 12, 20, 22].

Through the reciprocity of ray paths in Figure 2.4c, surface source signals from varying ranges arrive over a fan of angles at a deep receiver point. The impact of refraction lessens at closer surface ranges as signals propagate primarily in depth as opposed to range. Transmission loss (TL) plots for a 100 *m* deep source, calculated using the Ocean Acoustics Toolbox KRAKEN program [17], are shown in Figure 2.5. A TL plot shows the relative signal level as acoustic signals propagate in terms of signal loss from the initial level accounting for spreading and absorption [15]. TL is plotted with larger values equating to greater loss where the reference is the source level of 0 *dB*. The RAP is visible out to approximately 35 *km* in Figure 2.5a. Figure 2.5b includes propagation to 150 *km* range showing the unreliable propagation of

convergence zones past the RAP. Between convergence zones past the RAP, signal from the 100 *m* source experiences significant TL, effectively showing the limited viewing range of a receiver placed near the deep ocean bottom. A target moving above a deep receiver would be visible from overhead, out to 35 *km* in all directions.

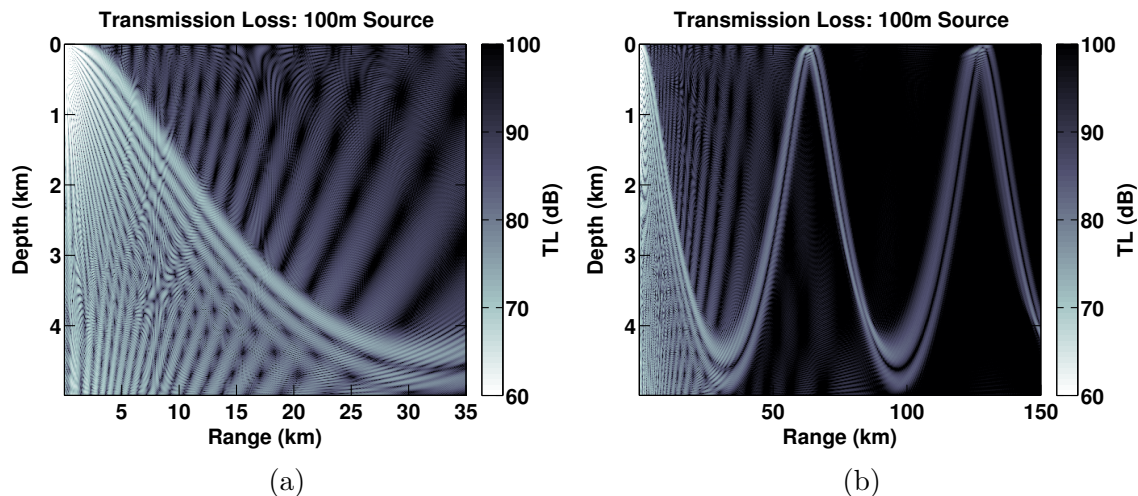


Figure 2.5: Deep ocean TL simulation created using the Ocean Acoustics Toolbox KRAKEN program [17] with the Munk sound speed profile from Figure 2.3b. Solutions computed using source frequency of 150 *Hz*. (a) TL plot for 100 *m* source propagating to 35 *km* showing RAP to deep ocean bottom. (b) TL plot for 100 *m* source propagating to 150 *km* range showing convergence zones from deep sound channel refraction.

2.2.3 Deep Ocean Noise

The low attenuation and ductal propagation of acoustic waves in the ocean can cause ambient noise to reach very high levels and contend with passive target signatures. Active sonar systems can be used to increase signal levels and provide the ability to match filter received signals with a transmitted waveform. However, in certain

cases such as when submarine stealth is required, active sonar cannot be utilized as it gives away submarine position, making passive sonar necessary. In the passive case, ambient ocean noise contends with desired target signature strength [15].

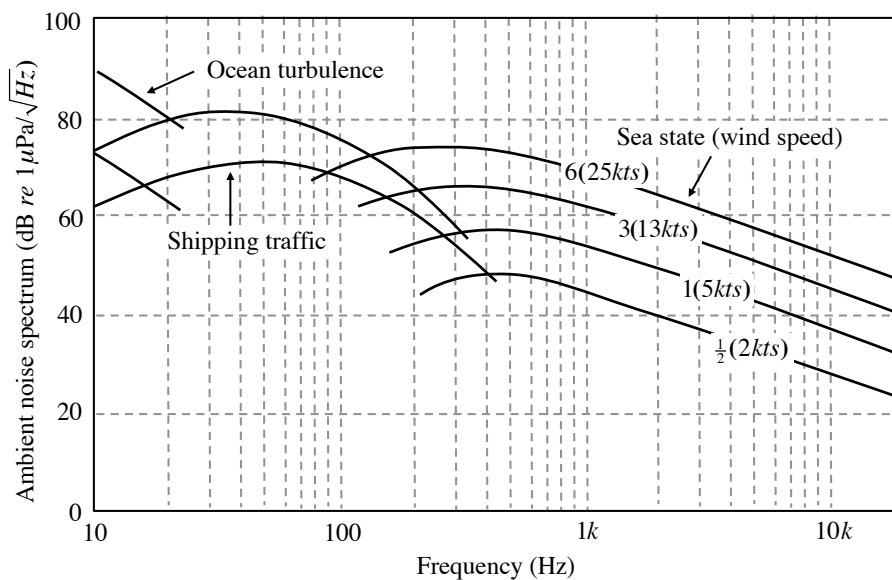


Figure 2.6: Characteristic deep ocean ambient noise spectrum adapted from Kinsler [15]. Ambient noise levels show possible ranges from shipping traffic and sea state. Wind speeds are indicated in knots (*kts*).

An example of the ambient noise spectrum present in the deep ocean adapted from Kinsler [15] is shown in Figure 2.6. The largest noise contribution occurs at very low frequencies with ocean turbulence. Shipping traffic causes elevated noise levels for frequencies up to a few hundred Hz . Low-frequency emissions propagate long distances and interfere with desired detection of nearby targets. Above $1 kHz$, surface and wind noise becomes the primary contender and reduces in spectrum level

with increased frequency.

An analysis from Gaul *et al.* [11] on experimentally acquired data, focuses on the effect of noise in the deep ocean below the critical depth. From the refraction around the deep sound channel axis, waves propagating long distances are effectively confined to the area above the critical depth, thereby reducing the presence of distant noise. The results compiled by Gaul *et al.* included experimentally gathered noise measurements below the critical depth and simulated transmission loss, using the measured sound speed profile, for distant shipping sources. Overall, the results indicate a reduction in noise below the critical depth for both shipping and wind noise as shown in Figure 2.7. Further, simulation of transmission loss from surface ships at varying ranges shows a significant reduction in 50 *Hz* received spectrum level with increased range.

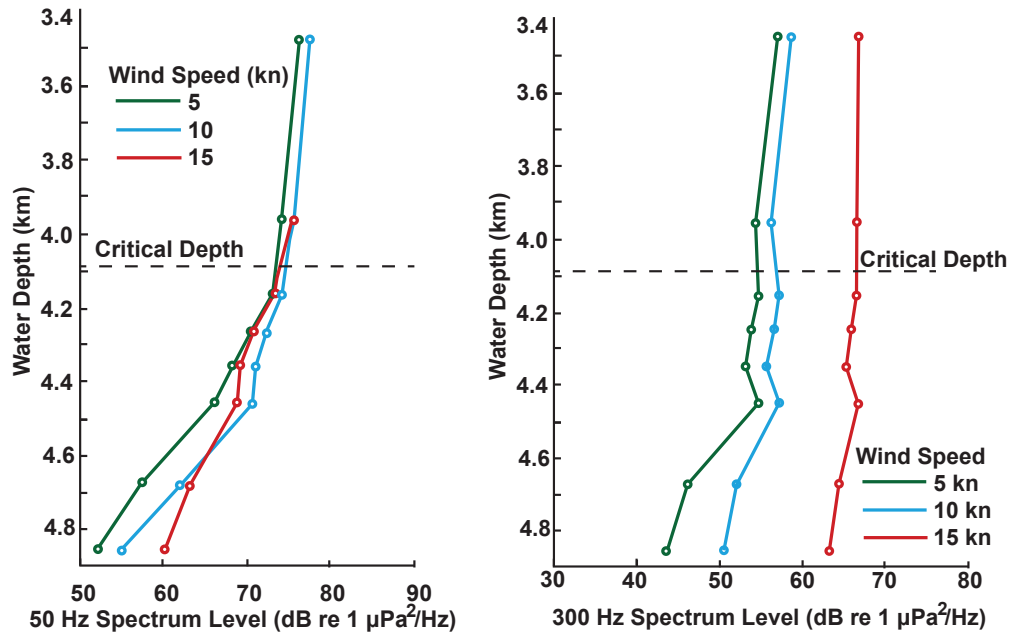
At the minimum surface range shown in Figure 2.7c of 200 *km*, the transmission loss with depth is approximately 5 *dB*. Further ranges show substantially increased transmission loss including 20 *dB* for a ship simulated at 1500 *km*. Li *et al.* [12, 13] simulated wind noise using the measured sound speed profile used by Gaul *et al.* showing agreement with the experimentally acquired data. The measured sound speed profile placed the critical depth at 4.1 *km* and the bottom depth at 4.9 *km*. As seen in Figure 2.7a, there is a reduction in the 50 *Hz* wind noise level from the critical depth of 15 *dB* at the ocean bottom. Similarly, there is a reduction in the 300 *Hz* wind noise spectrum level that is most pronounced for 5 *kts* wind with a

10 *dB* reduction from the critical depth. Li *et al.* also presented similar results for distant shipping noise based on the Historical Temporal Shipping (HITS) database [23] supporting that distant shipping noise reduced significantly (25 *dB* in Li's case) compared to the noise level at the critical depth.

As seen in Section 2.2.2, deep placement of receivers allows the exploitation of the RAP from near surface sources. Applying the results presented by Gaul *et al.* and Li *et al.*, ideal placement of passive deep receivers is below the critical depth, near the ocean bottom. In addition, preserving the arrival angles of signals within the RAP yields a spatial separation of sources near the surface that will be further explained and utilized in Chapter 6.

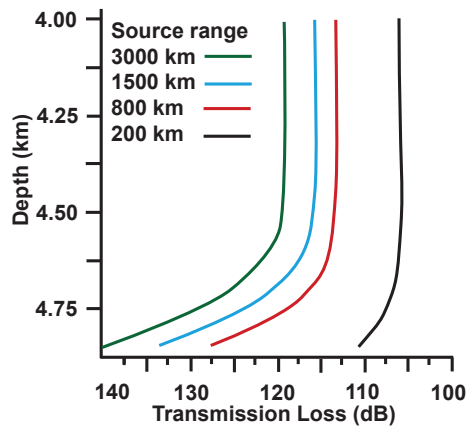
2.3 Normal Mode Model

Normal mode theory in ocean acoustics is an alternative to using ray methods, such as those used in the BELLHOP program [10]. Normal mode solutions allow for direct calculation of pressure fields within the waveguide as opposed to fully tracing all arrival paths from a source with a ray tracer algorithm. However, due to the limited applicability of the modal solutions to a single sound speed profile, ray tracing algorithms afford more flexibility in simulating a range-varying environment such as propagation from the deep ocean onto the continental shelf. In this case there is a sound speed shift from deep ocean to shallow water and a range dependent bathymetry. Normal modes also offer the ability to calculate the fields from multiple



(a)

(b)



(c)

Figure 2.7: Deep ocean noise plots adapted from Gaul *et al.* [11]. (a) Wind noise measured below critical depth at 50 Hz. (b) Wind noise measured below critical depth at 300 Hz. (c) Simulated distant shipping noise at 50 Hz for surface ships at variable range.

source depths at many receiver ranges using a single set of modal solutions, whereas ray tracing must be re-computed for each specific source with arrivals for each receiver location.

The normal mode theory is employed in the Ocean Acoustics Toolbox KRAKEN program [17]. Solving for pressure fields from a time-harmonic point source at known receiver locations begins with solving the depth dependent, two-dimensional Green's function in cylindrical coordinates,

$$(\nabla^2 + k^2)p = \delta(r)\delta(z - z_s). \quad (2.5)$$

∇^2 is the Laplacian, k is the wavenumber, p is the pressure, and the delta functions indicate the source point is located at a depth z_s in a cylindrical coordinate system with axial symmetry. Solving for the pressure and utilizing separation of variables at a single radial frequency ω yields,

$$p(r, z, \omega) = \frac{i}{4\rho(z_s)} \sum_{m=1}^{\infty} \Psi_m(z_s)\Psi_m(z)H_o^{(1)}(k_{rm}r), \quad (2.6)$$

where $\rho(z_s)$ is the density at the source point, Ψ_m is the m th mode function for the $k_m r$ horizontal wavenumber component, z_s is the source depth, and $H_o^{(1)}$ is the Hankel function of the first kind, appropriate for the $e^{-i\omega t}$ time convention [14]. Using this result, the pressure can be solved for at any depth z and range r within the water

column where these modal solutions are valid. A single set of modal solutions is limited to environments that exhibit a single sound speed profile in the water column and the ocean bottom over the desired range extent. For range dependent environments, a computationally intensive method of coupling modal solutions is described in the KRAKEN documentation [17]. A set of modal solutions are also only valid for a single frequency. In order to simulate broadband sources, multiple modal solutions must be calculated at multiple frequencies according to the desired bandwidth. Modal solutions calculated at even frequency intervals can be reconstructed into time series data through inverse Fourier transform.

Chapter 3

Waveguide Invariance

This chapter presents the concept of waveguide invariance. The waveguide invariant is a scalar parameter that characterizes the interference structure of acoustic propagation in an ocean waveguide. This invariant parameter provides a relationship between the receiver to source range and the broadband frequency content of the source in a passive sonar context. For many shallow water environments, the waveguide invariant, β , has been seen to be close to unity with a distribution relating to variations in parameters such as sound speed, receiver and source depth, and bottom attenuation [6]. In deep ocean environments, however, the value of β is more sensitive to the range and frequency. Recent research [3, 4, 5, 6, 7, 8, 20, 24] on the presence of invariance striations in active sonar systems shows that the “active invariant” γ depends on the sonar geometry (source-target-receiver ranges) and the scattering function of the target.

3.1 The Passive Invariant

The passive scalar waveguide invariant parameter β derived by Chuprov [1] characterizes the slope ($\frac{\partial \omega}{\partial r}$) of interference patterns visible in spectrograms for moving targets as a function of range and frequency. For passive sonar, the sound pressure at range r and depth z due to a point source is written using normal mode theory as

described in 2.3. Substituting the asymptotic approximation for the Hankel function, the pressure is written,

$$p_0(r, z, \omega) = \frac{e^{i\pi/4}}{\rho(z_s)\sqrt{8\pi r}} \sum_{m=1}^{\infty} \Psi_m(z_s)\Psi_m(z) \frac{e^{ik_m r}}{\sqrt{k_m r}}, \quad (3.1)$$

where z_s is the depth of the source, $k_m = \omega/v_m$ is the real wavenumber of the m th propagating mode, v_m is the phase velocity of the m th mode, and Ψ_m is the depth-dependent mode function. The acoustic intensity from this pressure field can be written as [2],

$$I_0(r, z, \omega) = \sum_m \sum_n B_{mn} \cos((k_m - k_n)r), \quad (3.2)$$

where B_{mn} are the modal amplitude coefficients. The above expression of the intensity can be interpreted as a function of range, depth, and frequency. Specifying a receiver depth, the waveguide invariant is calculated by solving for the values of range increment ∂r and frequency increment $\partial \omega$ such that a simultaneous change in each dimension gives a constant acoustic intensity. The constant intensity striations in the range-frequency spectrogram are described as

$$\frac{d\omega}{dr} = \frac{\partial I / \partial r}{\partial I / \partial \omega}. \quad (3.3)$$

After some manipulation [1, 2], the definition for the passive invariant β is written as,

$$\beta = \frac{r}{\omega} \frac{\partial \omega}{\partial r}. \quad (3.4)$$

Figure 3.1 includes a passive spectrogram and range plot for a small craft recorded on a single hydrophone on the Columbia River, OR. The boat range plot indicates a minimum range to the receiver of 20 m at the closest point of approach (CPA). The spectrogram is shown for frequencies below 10 kHz. The invariance striations visible exhibit a curvature similar to the source-receiver range as the boat travels past the hydrophone location. The change in striation slope with the change in range is easily visible in this case.

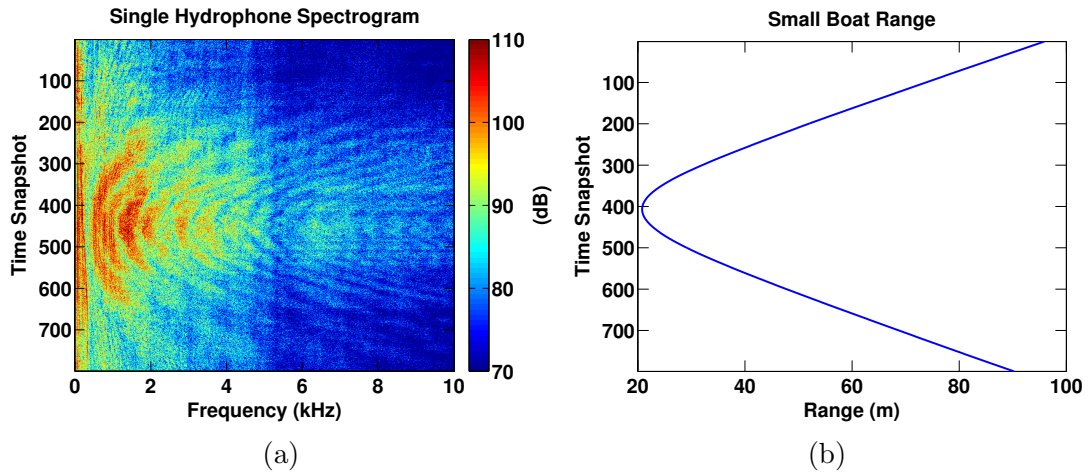


Figure 3.1: Acoustic data recorded by the NEAR-Lab on the Columbia River, OR, of a small boat traveling past a single hydrophone. (a) Spectrogram of acoustic data exhibiting invariance striations changing in slope and spacing with source range. (b) Small boat range to receiver showing symmetrical curvature similar to spectrogram striations.

3.2 The Active Invariant

The idea of the waveguide invariant presented by Chuprov suggests that the propagation of acoustic waves in an ocean waveguide environment could be characterized by a single scalar parameter that is robust to environmental variation. This waveguide invariant β was described initially in relation to passive sonar. In the case of active sonar, the waveguide invariant has been proposed and demonstrated to include two-way propagation and target scattering [3, 4, 5].

A factor limiting the performance of active sonar is not the presence of ambient noise from Figure 2.6, but reverberation and clutter from the transmitted pulse that interferes with the ability to identify desired targets. Extending the invariance phenomenon to the interference structures in received active signals could be used to enhance the performance of active tracking algorithms [20, 21]. Exact features such as sound speed, bathymetry, and bottom properties are rarely known to the degree required to fully compensate for the effects of the environment. The active waveguide invariant was derived by Zurk *et al.* to include the effects of two-way acoustic propagation using a similar approach to that applied by Chuprov for the passive case. The derivation includes the effect of two-way propagation, transmitter-target and target-receiver, as well as the scattering function of the target [25]. After manipulation of the acoustic intensity derived for active geometry [3], the active invariant is written

as,

$$\gamma = \frac{\beta}{1 + \frac{r_d}{r}\zeta}, \quad (3.5)$$

where $r = r_1 + r_2$ is the bistatic range (source-target-receiver), and $r_d = r_1 - r_2$ is the range difference. ζ is a function of the group velocities of the influencing modes and the scattering functions. A comprehensive derivation of γ can be found in Quijano *et al.* [5]. The significant result is that for monostatic geometries ($r_d = 0$), equation 3.5 predicts that $\gamma = \beta$.

Chapter 4

Array Processing

As described in Chapter 2, acoustic waves propagate through ocean environments with a dependence on the sound speed profile. When an acoustic signal is received far enough from the source that the curvature of spreading from the source can be neglected, the received signal can be approximated as plane waves. It is often advantageous to resolve the plane wave arrivals in terms of arrival angle as well as arrival time. This chapter presents the concept of using an array of sensors to sample received waveforms spatially as well as in time and the concept of beamforming to calculate the direction of signal arrivals.

4.1 Array Geometry

The two array geometries discussed in this thesis are the horizontal line array (HLA) and the vertical line array (VLA) as seen in Figure 4.1. Array elements are assumed to be equally spaced with an inter-element spacing d with $d = \lambda/2$ where λ is the wavelength at the design frequency f_d . The design frequency is chosen in order to resolve a specific target frequency. This thesis considers a design frequency for active sonar between 1 and 10 kHz whereas passive is limited to below 1 kHz . The minimum sampling frequency f_s to satisfy Nyquist requirements in time is $f_s = 2f_d$.

In the case of a towed HLA, signals arrive at bearing angle ϕ ranging from 0°

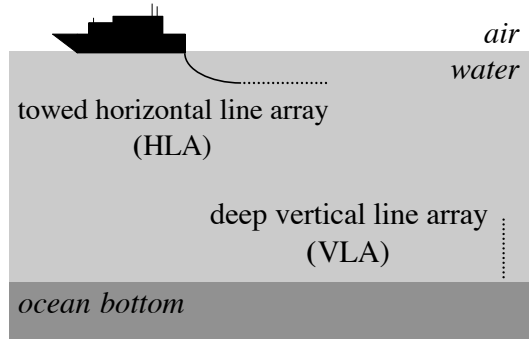


Figure 4.1: Diagram showing array placement for towed horizontal line array (HLA) and deep vertical line array (VLA).

(forward) to 180° (aft). These two extremes in bearing angle are termed end-fire. For a deep VLA, arrival angles are differentiated from HLAs by using the convention of vertical angle θ ranging from 90° for signals arriving from directly overhead and -90° for end-fire arrivals from below.

4.2 Conventional Beamforming

For an array of hydrophones in the far-field of a source, plane waves are received with a time delay dependent on the angle of incidence on the array aperture. This delay is shown in Figure 4.2 using the convention of bearing angle ϕ for a towed HLA from Section 4.1. Array timeseries data $x(t)$ is recorded as separate channels for N total elements. Once the recorded time series data is converted to the frequency domain, time delay between array elements equates to a frequency-dependent phase shift [26]. The conventional beamformer utilizes the phase delay between array elements introduced by the plane wave angle of incidence.

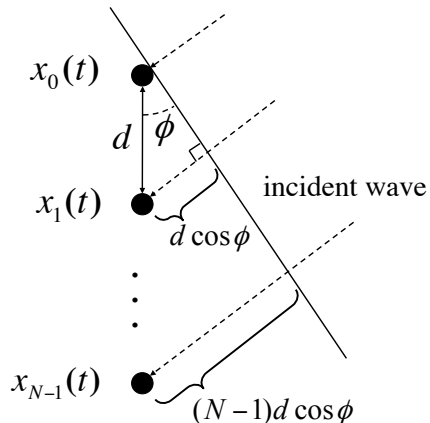


Figure 4.2: Diagram of delay between array elements of an incident plane wave with inter-element spacing d , incident angle ϕ , and N total array elements. $x_{n-1}(t)$ represents the recorded acoustic data for the n th of N total array elements.

Keeping with the HLA bearing convention, the beam response for a single bearing angle is formed by accounting for the delay between array elements and coherently summing the array data [26]. Calculating the beamformed output $B(\phi, f)$ using conventional frequency domain beamforming first requires converting time series data to the frequency domain through the Fourier transform. The beamformer output $B(\phi, f)$ for a single frequency is computed as power for the arrival angle ϕ with,

$$B(\phi, f) = |w^H(\phi, f)x(f)|^2. \quad (4.1)$$

$x(f)$ is the $N \times 1$ data vector for a single frequency recorded at each hydrophone and $w(\phi, f)$ is the $N \times 1$ weighting vector that contains the phase shift between sensors for each bearing angle. The superscript H denotes the Hermitian matrix transpose.

The beamformer weighting vector can be written using the phase convention shown in Figure 4.2 as,

$$w(\phi, f) = [1 \ e^{i2\pi\frac{f}{c}d\cos(\phi)} \ \dots \ e^{i2\pi\frac{f}{c}(N-1)d\cos(\phi)}]. \quad (4.2)$$

Calculating $B(\phi, f)$ for ϕ ranging from 0° to 180° will give the complete beamformed output at the frequency f . When broadband beamforming is desired, the beamformer calculation must be repeated over the desired frequency band.

The Fourier transform step in the frequency domain conventional beamformer requires taking finite segments of the time series data called snapshots. Snapshot length is selected based on the desired frequency resolution of the Fourier transformed signal and often limited by the type of sonar being used. For active sonar, specifically in application to waveguide invariance, long snapshots including multipath echoes of a transmitted waveform will preserve the broadband interference structure. For passive sonar, selecting short snapshots allows a more continuous sampling in time at the cost of poor frequency resolution and reduced spectral power. For consecutive snapshots, the beamformed outputs can be plotted together as a contour showing power output, with respect to bearing angle, as a progression over time. The beamformer output in ϕ for an HLA plotted versus time is referred to as a bearing-time record (BTR). Using the VLA convention from Section 4.1, referencing vertical angle θ , the beamformer weight vector in equation 4.2 is calculated with a phase delay between array elements

as $d\sin(\theta)$ in place of the $d\cos(\phi)$ term in the case of the HLA. The beamformer output for a VLA plotted in time is called a vertical-time record (VTR) and is often scaled with $\sin\theta$. Vertical angle is referenced to array broadside indicating arrivals from $\theta = 90^\circ$ are directly above the array and $\theta = -90^\circ$ are directly below.

4.3 Invariance Striation Beamforming

Conventional beamforming, as described in 4.2, takes a single frequency from a Fourier decomposed signal and forms an output by coherently summing the received hydrophone signals with a phase shift for a specific bearing angle. In the presence of waveguide invariance striations, the single-frequency beamformer processes the array data including constructive and destructive interference. A method for striation-based conventional beamforming, derived by Zurk and Rouseff [7, 8], processes the array data with variable frequency to align with the spectrogram striations. The frequencies along striations present in array spectrograms are given by the difference in frequency Δf between hydrophones,

$$f_n = f_o + n\Delta f, \quad (4.3)$$

where f_n is the frequency along the striation at each array element, f_o is the starting frequency, and n is the n th of N total elements in the array.

Using the change in frequency between phones, we can rewrite the passive waveguide invariant β from equation 3.4,

$$\beta = \frac{\Delta f}{\Delta r} \frac{R}{f_o}, \quad (4.4)$$

where Δr is the change in range from source across the array and R is the geometric range from array to source. In circumstances where the range R and the target bearing ϕ_t are known and β is desired, spectrogram striations can be used to complete the waveguide invariant calculation. The bearing of the source gives the change in range between array elements similar to Figure 4.2,

$$\Delta r = d \cos \phi_t. \quad (4.5)$$

The weighting vector for conventional beamforming, described in equation 4.2, compensates for the phase shift from the delay between array elements assuming the received data has a constant phase over the array. Including the variable frequency in the suggested striation beamformer introduces an additional phase difference between hydrophones based on the phase over the bandwidth of the received waveform. In order to compensate for this waveform phase, an additional phase term $\hat{\psi}$ [7] is added to the conventional beamformer steering weight from equation 4.1 where the modified

weights for the n th of N elements is,

$$w_n(\phi, f_n) = e^{-i\hat{\psi}n\Delta f} e^{i2\pi\frac{f_n}{c}(n-1)d\cos(\phi)}. \quad (4.6)$$

Implementation of the striation-based beamformer can preserve the spectrogram striation pattern in a broadband calculation. Preserving the progression of striation shifts in frequency over time can provide enhanced tracking abilities by adding a frequency hypothesis related to range as proposed by He *et al.* [20, 21]. From the conventional output, the only tracking ability comes from change in target bearing with time. The striation pattern seen in the spectrogram will change in frequency and spacing as a target changes range at the same bearing angle.

Chapter 5

Simulation and Analysis

This chapter presents simulated sonar array data using normal mode theory to calculate pressure fields at array element locations. The Ocean Acoustics Toolbox KRAKEN normal mode program [17] is used to solve for the modal solutions to the ocean waveguide problem as described in Section 2.3. The pressure at each array element is then calculated from the modal solutions over a bandwidth with equation 2.6 [14] for a bandwidth of frequencies for element coordinates in r and z . Plotting the frequency spectrum for each array element reveals waveguide invariance striations. Simulated data for and HLA in moderate water depth and a VLA in deep water are presented showing interference striations. A method for extracting invariance striation slopes is presented that incorporates the Radon and Fourier transforms resulting the extraction of striation slope and intuitively further separating striations in spacing. This proposed method is applied to the simulated HLA and VLA data.

5.1 Automatic Striation Extraction

The passive waveguide invariant can be calculated if all variables from equation 3.3 are known. Similarly, this can be done for active sonar using equation 3.5. When the environment has not been characterized, it is often desirable to extract the slope $\frac{\Delta\omega}{\Delta r}$ from experimental data using the striations as they appear in spectrograms. Under

some circumstances, striations are clearly visible and can be measured from the array frequency power spectrum. In an ideal case, all striations are visible from all sources and are resolvable from one another. In many cases, poor signal level or multiple sources cause the striations to become noisy and unresolvable from one another. When striations cannot easily be found by visual examination, image processing techniques for automatic striation analysis must be applied.

Processing techniques have been proposed for extracting striation slopes concurrent with the initial invariant derivation of Chuprov [1]. Proposed methods include canny edge detection [27, 28], two-dimensional Fourier transforms [29], and Radon transforms [24]. Each of these methods allows calculation of a distribution of striation slopes solely based on spectrogram image analysis. The extent to which these methods have been applied has been largely limited to extracting the striation slopes.

While edge detection methods have the potential to precisely track striations in a spectrogram, they are limited by image noise and resolution. Calculation of the slopes associated with detected edges also requires secondary processing. Fourier transform-based methods are also limited by image resolution but provide the ability to characterize repeating structures such as striation interference patterns. The Radon transform can be used to directly distinguish linear features in slope with limited susceptibility to noise. In this thesis, a method utilizing the Radon transform is enhanced by the further processing of a Fourier transform for each radial projection to add a distribution of the striation spacing.

Applying a Fourier transform along each row of the projected result will yield peaks corresponding to preserved harmonic content from spectrogram images containing parallel striations with periodic spacing. The process of Fourier transforming a Radon transform at all radial angles is equivalent to the two-dimensional Fourier transform through the projection-slice theorem [28]. Expanding the process into two steps allows for intuitively separating harmonic content in angle, then further separating it by spacing. Directly applying a two-dimensional Fourier transform yields a similar result without the option to select specific projection angles for further analysis.

The Radon transform projects an image over radial angle and can be used to separate linear structures in angle. An example of the Radon transform projection for a test image is shown in Figure 5.1a. The image is square and contains three lines: two with 135° slopes and one with a 45° slope. The image origin is set at the center: $X = 0$ and $Y = 0$. In the Radon projected result (Figure 5.1b) rows correspond to the projected image for 1° to 180° rotation around the origin. When the original image is projected along the slope of a linear feature, the result is a peak with offset related to the radial distance from the image center. In Figure 5.1a, the single line with 45° slope is offset from the image center and the projection at 45° exhibits a peak at 6 on the horizontal axis in Figure 5.1b. The important result in this example is that the parallel set of lines yield two spots at the corresponding 135° projection angle with perpendicular spacing preserved.

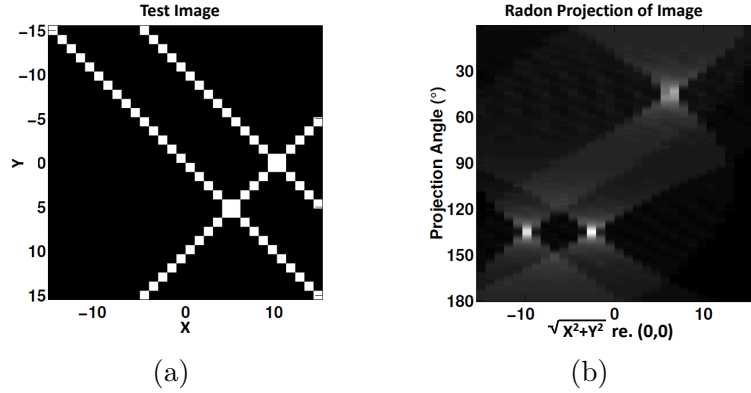


Figure 5.1: Radon projection example illustrating localized peaks associated with sloped lines. (a) Test image containing two lines with 135° projected slopes and one with a 45° slope. (b) Radon transformed test image from (a) showing peaks corresponding to the slopes of the lines present. The two parallel lines with 135° projected slope occur at the same projection angle with radial distance from the origin of the test image preserved.

For spectrograms exhibiting linear striations, a projection along the radial angle corresponding to striation slope preserves the structure of the interference. Projecting the spectrogram over radial angles that do not align with striation slopes sums across the peaks and nulls of the interference pattern, spreading out the projected result and reducing the presence of harmonic content. In the test image example, the perpendicular spacing S_\perp of parallel lines is preserved in the projection. In order to find spacing in a single dimension of the original image, the projected spacing must be scaled with the projection angle. The projection angle Θ is related to the image dimensions by $\Theta = \tan^{-1}(\frac{X}{Y})$. The spacing in the X -dimension of the image S_x can then be calculated with $S_x = \frac{S_\perp}{\cos \Theta}$. For simplicity, the Fourier transform of the Radon transform output will have a spacing axis scaled in S_\perp .

In order to illustrate the proposed striation slope and spacing extraction method,

a simulated monostatic active sonar spectrogram image containing striations was created using the Ocean Acoustics Toolbox KRAKEN program [17]. Pressure fields were calculated to include two-way propagation for a towed HLA geometry with $N = 100$ elements using a downward refracting profile [18] for 2 *km* water depth and 300 to 500 *Hz* bandwidth. The target was modeled with a unity scattering function at a range of 23 *km* and bearing angle $\phi = 165^\circ$ with respect to the array convention defined in Section 4.1. The array element spacing was set for a design frequency of 2 *kHz* to 0.375 *m* at a depth of 100 *m*. The phone-frequency spectrogram is shown in Figure 5.2a. The corresponding Radon transform in Figure 5.2b has been scaled with slope Δf over the array by $\tan \Theta = \frac{\Delta f}{Array}$, where Θ denotes the projection angle. The harmonic content from the spectrogram striations preserved in the Radon projection output is visible with the same perpendicular spacing as seen in the original spectrogram image change in frequency of -8 *Hz* over the array.

With the harmonic content preserved in the Radon transformed result, a Fourier transform can be applied to each projection angle. Peaks correspond to the slope and spatial frequency of the striations present in the original image. Figure 5.2c shows the result of the Fourier transform with the scaled slope axis and a labeled horizontal axis indicating the expected location of peaks corresponding to wide and narrow striations. The feature in the Fourier transformed result relating to the visible striations in Figure 5.2a is a very narrow peak corresponding to a frequency slope of -8 *Hz* over the array. Scaling the perpendicular spacing to spacing in frequency

based on the projection angle yields a striation spacing of 18 Hz . In the case of the phone-frequency spectrogram, projection angle includes components of phone and frequency with $\Theta = \tan^{-1}(\frac{\Delta f}{Array})$. The spacing of 18 Hz includes only the frequency dimension as demonstrated in the test image example shown previously.

The low-frequency content of the spectrogram image is concentrated on the left hand portion of Figure 5.2c, spread over the extent of the projections. This is caused by the reduction in spectral power with increased frequency for all phones in the phone-frequency spectrogram. Because the striations are clearly visible in the spectrogram image, the Radon transform was limited in projection angle from 0° to 20° with counter-clockwise rotation. With increased rotation, the low-frequency content is no longer preserved. Even in this case where striations are clearly visible in the spectrogram, variations within the image will appear in the Radon projected and Fourier transformed output. Proper normalization of this result gives a distribution of β values present in the image.

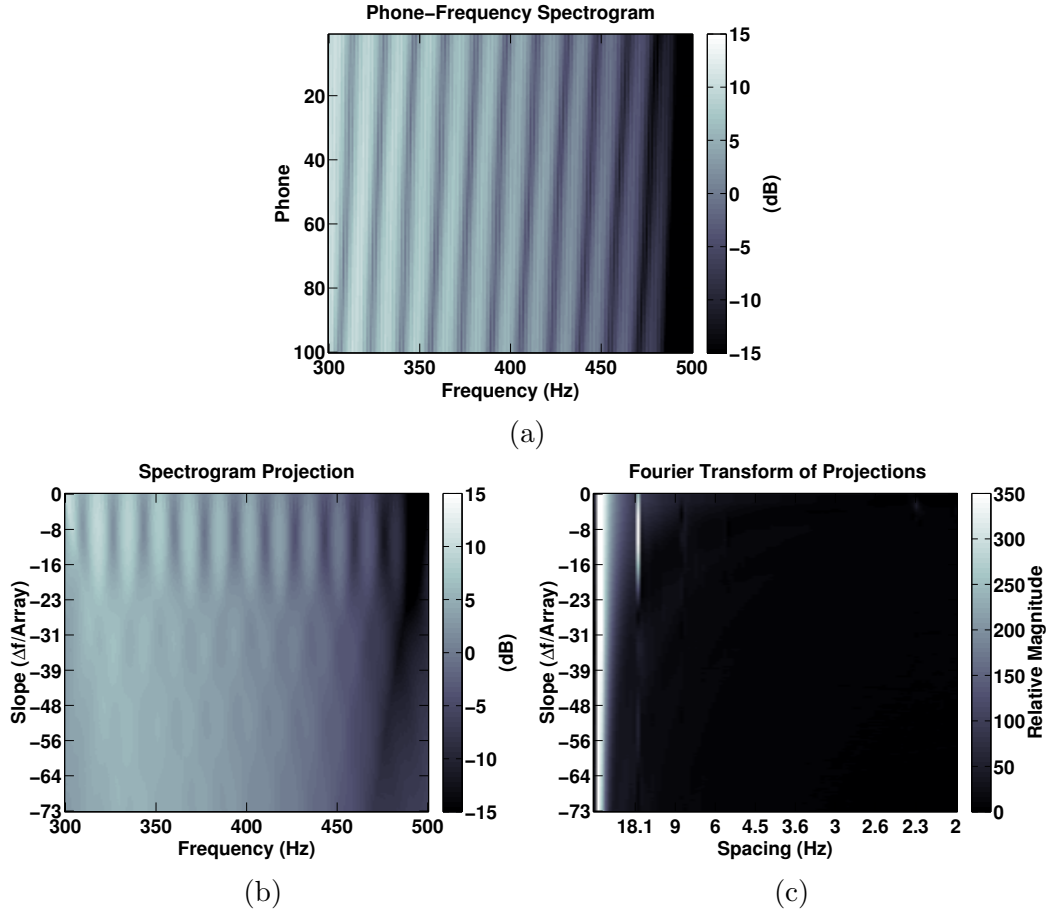


Figure 5.2: Striation slope extraction with Radon transform and Fourier decomposition. (a) Spectrogram of simulated snapshot received on hydrophone array. Invariance striations are visible in body of spectrogram. (b) Radon transformation of the phone-frequency spectrogram over a selected range of radial angles with a scaled slope given as change in frequency Δf over the array. (c) Fourier decomposition of each projected slope yields a peak corresponding to the slope and spacing of the striations from the array spectrogram. Spacing axis is scaled for 0° projection angle.

5.2 Horizontal Line Array

A monostatic, active HLA simulation is shown in Section 5.1 with waveguide invariance striations extracted based on the proposed Radon and Fourier transform

methodology. The Radon projected, Fourier decomposed data containing a single peak corresponding to the slope and spacing of the striation pattern is shown in Figure 5.2c. For the spectrogram of the frequency content of the return pulse in Figure 5.2a, the striation slope was calculated to be -8 Hz over the array.

Beamformer plots for the conventional beamformer, the phase-uncompensated striation-based beamformer, and the phase-compensated striation beamformer from Section 4.3 are presented in Figure 5.3. In order to estimate the phase compensation $\hat{\psi}$ for the striation-based beamformer, the change in phase over frequency for each array element was calculated. The change in phase with frequency was approximately linear and consistent over all elements. Comparison of the three beamformer plots show the necessity of the phase-compensation term from equation 4.6. Using the conventional beamformer output as a reference bearing, the phase-compensated striation-based beamformer resolves the target angle appropriately at 160° . The uncompensated striation-based beamformer focuses maximal output near 180° which does not match the expected result. Using the conventional beamformer target bearing $\phi_t = 160^\circ$ and equation 3.5 for a monostatic active system, the active invariant is calculated as $\gamma \approx 13$ from the simulated target range $r = 23 \text{ km}$, angular frequency $\omega/2\pi = 400 \text{ Hz}$, and $\Delta r = Nd \cos \phi_t$.

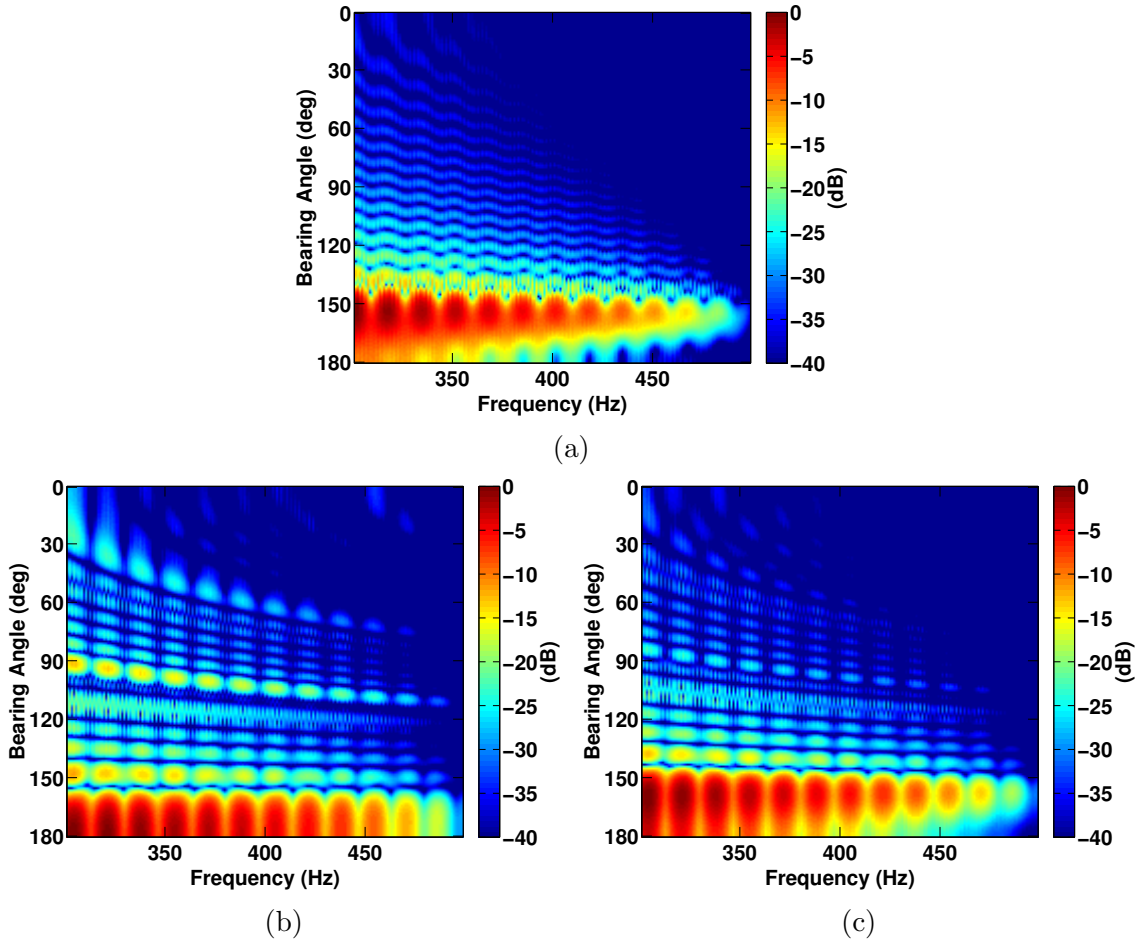


Figure 5.3: Simulated broadband beamformer plots shown with 40 *dB* dynamic range referenced to the maximum output. (a) Conventional beamformer output giving target bearing at 160°. (b) Striation-based conventional beamformer without phase-compensation term indicating target presence near 180°. (c) Striation-based conventional beamformer with phase-compensation showing a corrected target bearing and preserving striation pattern within beamformer output.

Cuts through the beamformer maximum bearing across frequency for the conventional and the phase-compensated striation-based beamformer are plotting together in Figure 5.4a. The striation-based beamformer preserves the striations throughout the entire frequency range, whereas the conventional single-frequency result blurs the

striations together especially for higher frequencies in the simulated band. Direct calculation of the original phone-frequency spectrogram slopes in Figure 5.2a yields increasing slope with increasing frequency as expected from the definition of γ from equations 3.4 and 3.5. In the monostatic case where the transmitter and receiver are co-located, γ has a linear dependence on frequency. Holding γ , r , and Δr constant (corresponding to a single snapshot in time) requires the $\Delta\omega$ term to increase with frequency, increasing striation slope with frequency.

While in this case, conventional beamforming at single frequencies can preserve some of the more vertical striations, it blurs the striations at higher frequencies exhibiting higher slopes. This conventional beamformer result preserves significantly more of the interference striations in comparison with the conventional result in Zurk and Rouseff [7], where the striation structure is not preserved in the cut through the beamformer maximum. This difference is partially attributable to the lower bandwidth of this simulation (Zurk and Rouseff’s publication specifies waveform in the 1 to 10 kHz mid-frequency sonar band) and the impact of environmental parameters on striation slope and spacing.

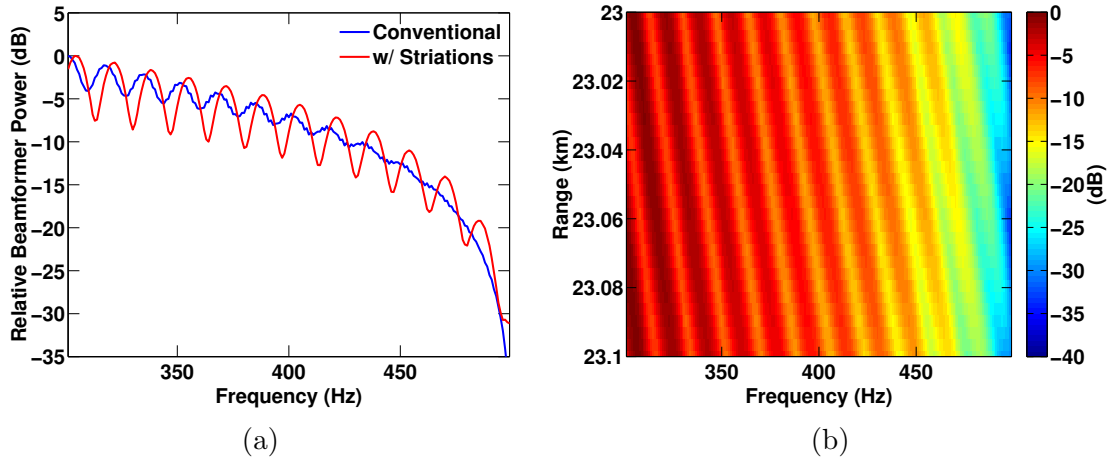


Figure 5.4: Cuts through the beamformer maximums showing preserved striation pattern. (a) Comparison between conventional and striation-based conventional beamformer outputs. Striation-based (red) preserves striation pattern over the full bandwidth compared with the smoothed output of the conventional single-frequency result. (b) Cuts through striation-based beamformer outputs with target simulated moving at 160° bearing from 23 km to 23.1 km in 3 m increments.

Plotting consecutive cuts through the maximum beamformer bearing with a target varying in range exhibits striations shifting in frequency as seen in Figure 5.4b. The peaks of the preserved striations can be traced as the target changes range from 23 km to 23.1 km while at constant bearing and constant velocity. Conventional bearing time records show target detections as tracks in bearing and time. While a target at constant bearing could be stationary, it could also be changing range without deviating from its bearing relative to the HLA. Utilizing the progression of these striations in time can give insight into the movement of a target further than the beamformer in bearing alone. In the previous work of He *et al.* [21], a method of utilizing the preserved striation patterns is proposed to enhance a Kalman filter

tracking algorithm.

5.3 Deep Vertical Line Array

As the concept of waveguide invariance has been studied primarily with respect to shallow water environments, its applicability to the deep ocean is largely limited by its dependence on the sound speed profile. While the classification of the waveguide invariant in deep water is largely unknown, interference striations are still present in array spectrograms. A deep VLA simulation using the Ocean Acoustics Toolbox KRAKEN program [17] for a moving source near the surface reveals striations similar to those seen in passive spectrograms of small boats recorded on a single hydrophone. Figure 5.5b shows a single hydrophone spectrogram for a 100 *m* deep source moving for directly overhead at constant velocity of 5 *m/s* to a surface range of 30 *km*. The receiver is simulated at 50 *m* from the ocean bottom. The overall shape of the striations follows a curvature similar in shape to the range of the source to VLA over time shown in Figure 5.5a. Invariance striations are also visible in phone-frequency spectrograms over the simulated 30-element array for a single snapshot in time. A phone-frequency spectrogram is shown in Figure 5.6a depicting the pressure fields caused by a source near the surface at a 11.8 *km* surface range.

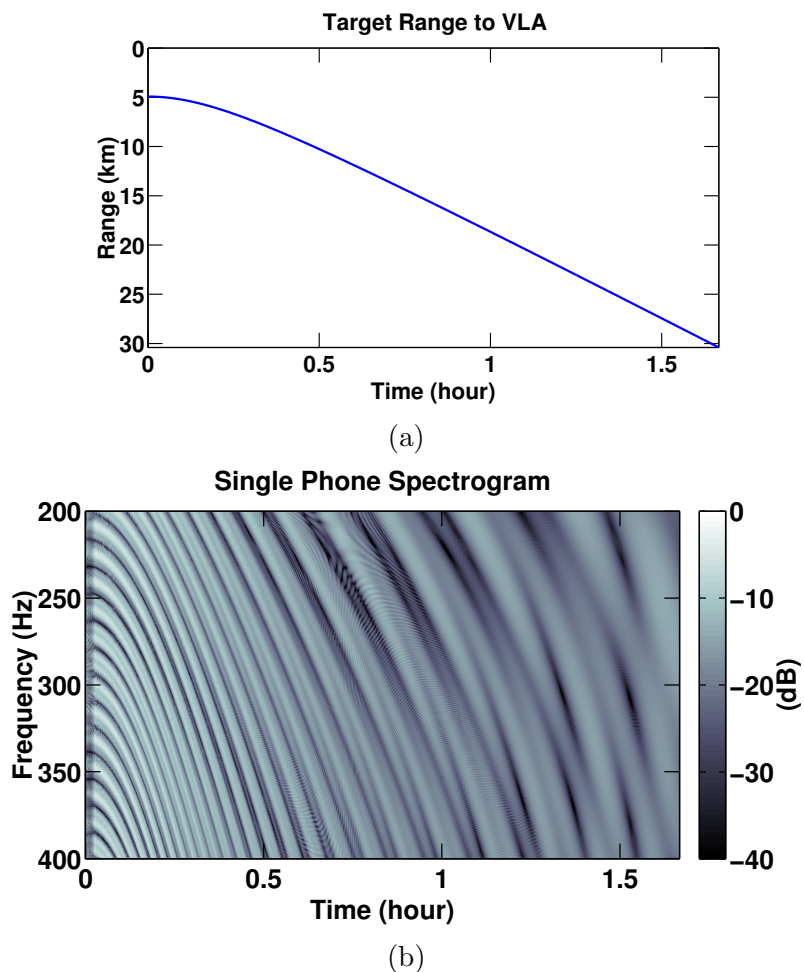


Figure 5.5: Deep VLA single hydrophone spectrogram simulated with Munk profile shown in Figure 2.3b. (a) Source-receiver geometric direct path range for 100 m source moving at a constant 5 m/s velocity and 4950 m receiver depth. (b) Single phone spectrogram limited to the simulated frequency band.

In the spectrogram from Figure 5.6a, multiple striation patterns are visible. Striation extraction was aided by the Radon transform and Fourier decomposition as outlined in Section 5.1 and output from all processing steps are shown in Figure 5.6. Layers of striations are tabulated for reference in Table 5.1, including slopes and spacing, and color-coded to match Figure 5.6d.

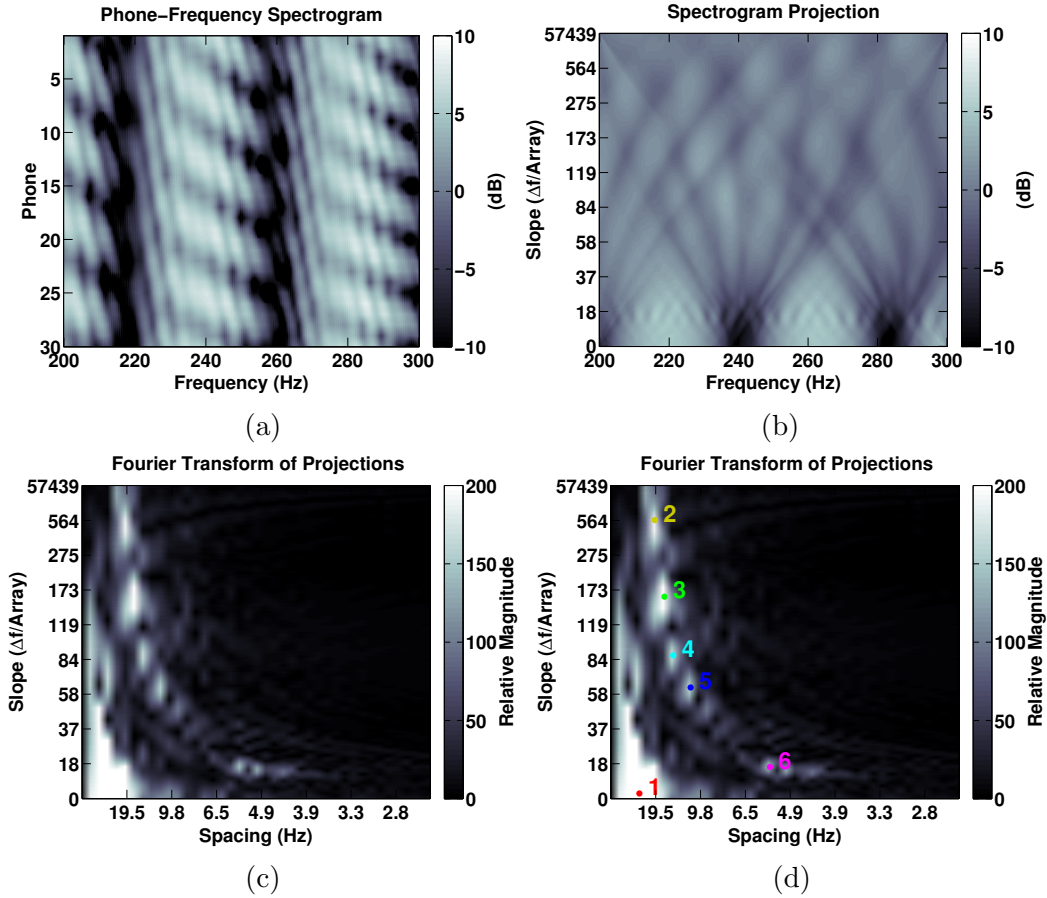


Figure 5.6: Striation slope extraction with Radon transform and Fourier decomposition. (a) Spectrogram of simulated snapshot received on hydrophone array. Invariance striations are visible in body of spectrogram. (b) Radon transformation of the phone-frequency spectrogram over a selected range of radial angles with a scaled slope given as change in frequency Δf over the array. (c) Fourier decomposition of each projected slope yields a peak corresponding to the slope and spacing of the striations from the array spectrogram. Spacing axis is scaled for 0° projection angle. (d) Fourier decomposition of each projected slope with local maxima marked. Associated slopes and spacing for the marked (color-coded) striation detections are recorded in Table 5.1.

Conventional beamforming preserves striation 1 in the beamformer output given there is no frequency change over the array. The conventional beamformer output is shown in Figure 5.8a exhibiting the direct path from the source at $\sin \theta = 0.3$ and the

Striation	Slope (Hz/Array)	Width (Hz)
1	0	40
2	410	20
3	155	19
4	88	14
5	63	11
6	12	5

Table 5.1: Detected striations in deep VLA simulation using the striation extraction method outlined in Section 5.1 and result presented in Figure 5.6. Slope is given as Δf , described in equation 4.3.

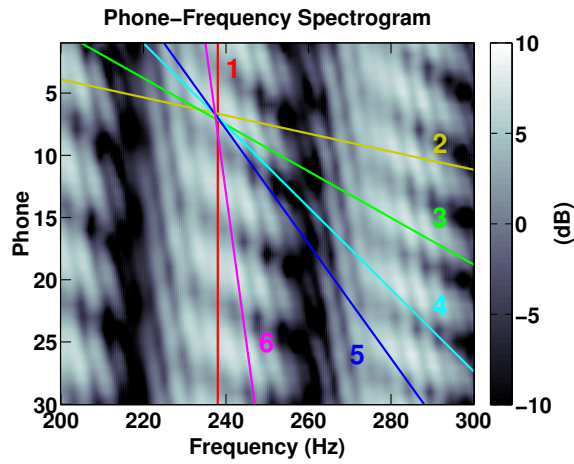


Figure 5.7: Spectrogram from Figure 5.6a including extracted slopes from Table 5.1 indicated as overlays.

bottom-bounce multipath at $\sin \theta = -0.3$. Extracted striations 2, 3, 4, and 5 are all caused by the interference within striation 1. As depicted in Figure 5.7, the extracted slopes for striations 2, 3, 4, and 5 align with the beating pattern at different radial angles. Narrower, step striations are also present in the spectrogram, appearing as small peaks in the upper-center of Figure 5.6c marked as striation 6.

Using the extracted slope for striation 6 in the striation-based beamformer methodology outlined in Section 4.3 preserves the 5 Hz spacing visible in the phone-frequency

spectrogram. The uncompensated striation-based beamformer result in Figure 5.8b exhibits an inconsistent target bearing over frequency that is not aligned with the conventional single-frequency result. The phase-compensated result in Figure 5.8c aligns the maximal beamformed response with the conventional result at $\sin \theta = 0.3$.

While striation 6 is easily visible in the phone-frequency spectrogram, it appears within the structure of striation 1. The cut through the maximal beam for the striation-based conventional beamformer preserves the presence of striation 6, but also contains the overall structure of striation 1 seen in the conventional single-frequency result shown in Figure 5.8a. Cuts through the maximal beamformer output for the single-frequency result and striation-based beamformer for the slope associated with striation 6 are included in Figure 5.8d. Extracted slopes for striations 2, 3, 4, and 5 were not included in striation-based beamforming due to the increased bandwidth required to be able to beamform along the entire slope extent.

This more complicated case of the invariance seen on a phone-frequency spectrogram, compared with the results shown in Sections 5.1 and 5.2, exemplifies the difficulty of extracting layers of striations from data containing multipath interference of multiple targets. Relating the concept of waveguide invariance to the striations seen in the VLA spectrogram image, it is apparent that this is a more complicated case than can be defined by a single scalar value for a source with a set range using equation 4.4. For a single phone-frequency spectrogram with bandwidth centered at f_o and neglecting refraction, R and Δr are set by the source-VLA geometry. These

constraints indicate that layers of interference striations with different slopes will each require a unique β or γ to satisfy equation 4.4. If a single invariant value truly characterizes the multipath interference in an environment, R and Δr must be determined for each unique striation slope, suggesting that the effects of refraction must be included in the calculation of propagation range. Exploring the full impact of refraction in relation to the scalar waveguide invariant is beyond the scope of this thesis and can be continued in future research.

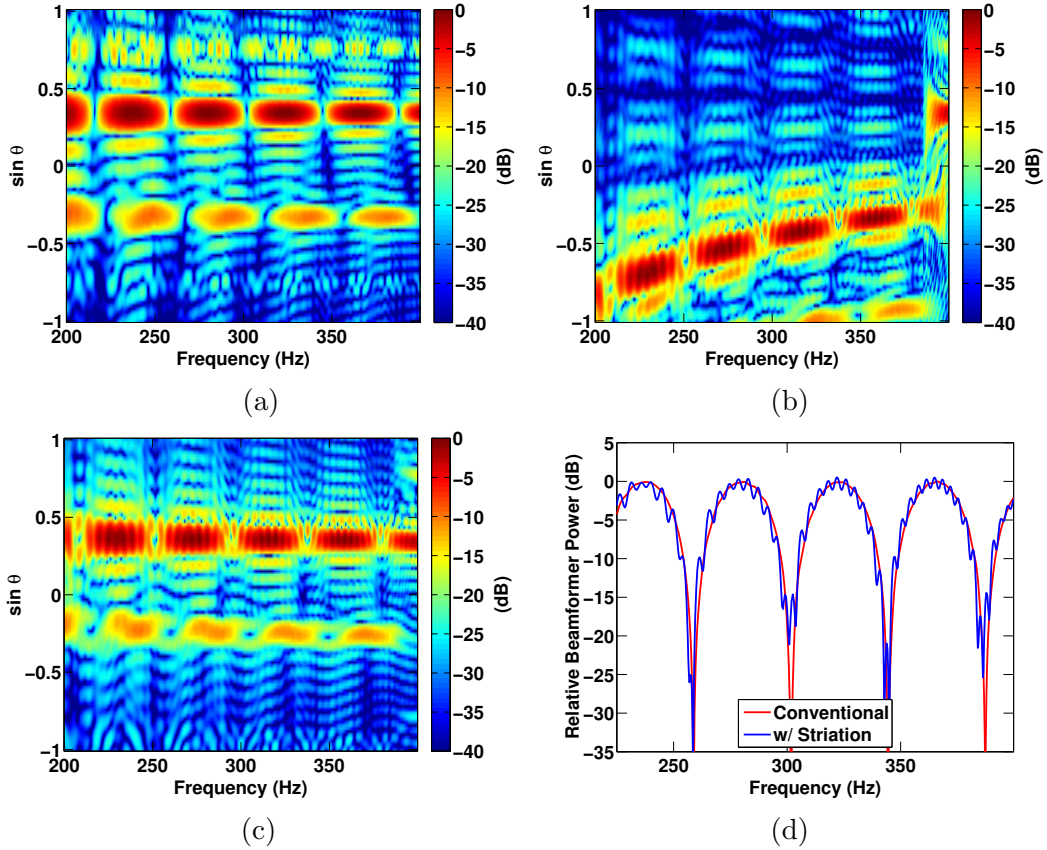


Figure 5.8: Vertical time record plots shown with 40 dB dynamic range for simulated VLA data. (a) Conventional beamformer output giving target $\sin \theta = 0.3$. Multipath reflection from the bottom bounce is visible below the broadside axis. (b) Striation-based conventional beamformer without phase-compensation term. (c) Striation-based conventional beamformer with phase-compensation showing a corrected vertical angle and preserving striation pattern 6 from Table 5.1. (d) Cut through maximum beam comparing conventional and striation-based result.

Chapter 6

Depth Based Signal Separation

The reliable acoustic path (RAP) phenomenon allows favorable propagation from shallow sources to nearby deep receivers as described in Section 2.2.2. VLA placement below the critical depth also has the advantage of reduced wind and distant shipping noise as addressed in Section 2.2.3 from the work of Gaul *et al.* [11] and Li *et al.* [12, 13]. Passive signatures from nearby interferers also appear on deep receivers with favorable RAP propagation and are difficult to differentiate from submerged sources since there is no horizontal aperture (all bearings arrive together). A method utilizing the interference structure associated with passive multipath from submerged sources is presented in the work of McCargar and Zurk [9] to separate nearby targets in depth. The depth separation methodology is presented with a simplified image theory derivation and applied to simulated data exhibiting depth dependent interference structure.

Traditional processing methods for deep VLAs involve beamforming over vertical angles and plotting target tracks as a function of time. The target range can be calculated based on the surface projection from the vertical angle of the target track. This chapter introduces methodology for separating targets in depth using a vertical angle versus time plot by utilizing harmonic interference patterns. Simulated results are presented for a submerged source and a nearby surface interferer.

6.1 Depth Based Signal Separation

Placement of acoustic sensors near the deep ocean floor can exploit the reduction in noise and propagation for nearby surface sources through RAP as presented in Sections 2.2.2 and 2.2.3 respectively. Further, implementing a VLA at the ocean floor can separate arrivals in vertical angle by beamforming over the array aperture. Using the image geometry depicted in Figure 6.1, it is apparent that nearby sources (marked as “interferer”) will arrive at the VLA with higher vertical angle θ as opposed to sources at greater surface range which will arrive at a lower vertical angle. In the case of a VLA, array broadside is specified to be a vertical angle of $\theta = 0^\circ$ and directly overhead is defined as $\theta = 90^\circ$.

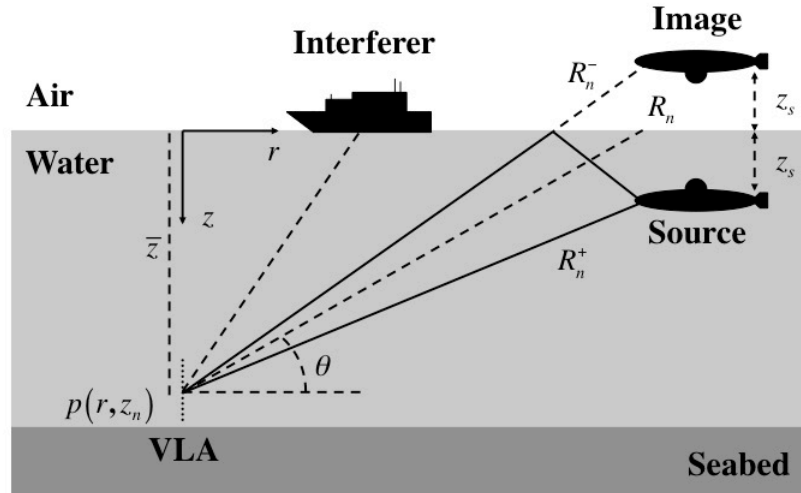


Figure 6.1: Diagram of image theory geometry indicating separation of a submerged source and the image reflected over the surface boundary. Sources are separated in vertical angle θ based on range.

In the far-field of the source and image dipole on the right side of Figure 6.1, the paths R_n^+ and R_n^- are irresolvable in vertical angle θ and they appear to arrive at each array element via the path marked as R_n . Due to the path difference between R_n^+ and R_n^- , the pressure field at the array caused by the image-source dipole will contain an interference pattern. Following the derivation from McCargar and Zurk [9], the pressure field from image-theory in a non-refracting isovelocity sound speed profile at the n th of N array elements is written,

$$\begin{aligned}
 p(r(t_l), z_n, \omega) &\approx S(\omega) \left[\frac{e^{ikR_n^+(t_l)}}{R_n^+(t_l)} - \frac{e^{ikR_n^-(t_l)}}{R_n^-(t_l)} \right], \\
 &\approx -2iS(\omega) \frac{\sin \theta(t_l)}{\bar{z}} e^{ik \frac{\bar{z}}{\sin \theta(t_l)}} \sin(kz_s \sin \theta(t_l)) e^{ik(n - \frac{N}{2})d \sin \theta(t_l)},
 \end{aligned} \tag{6.1}$$

where $S(\omega)$ is the spectral amplitude of the source signal, t_l is the snapshot in time, \bar{z} is the midpoint depth of the VLA, and the wavenumber $k = \omega/c$. The factor $\sin(kz_s \sin \theta(t_l))$ causes the interference pattern from the source and image dipole which increases in spatial frequency with source depth. This interference pattern is evenly spaced in $\sin \theta(t_l)$ and unevenly spaced in time. Beamforming over the array with the convention of vertical angle changes the steering vector delay terms in equation 4.2 from $d \cos \phi$ to $d \sin \theta$.

Simulated VTR plots of beamformed power output for sources at 1 m and 50 m depths are shown in Figure 6.2. Simulated data was created with direct calculation of pressure through equation 6.1 using a linear time axis, followed by beamforming in

$\sin \theta$. Figure 6.2c includes overlaid lines marking the nulls of the harmonic along the VTR trace for the 50 m source. The overlay illustrates the evenly spaced harmonic in $\sin \theta$ and uneven spacing in time. Taking a cut along the target trace in the VTR and using the pressure calculated from image theory in equation 6.1, the VTR power is given by,

$$P(\omega, \sin \theta(t_l)) \approx 2 \left(\frac{S(\omega) \sin \theta(t_l)}{\bar{z}} \right)^2 [1 - \cos(2kz_s \sin \theta(t_l))]. \quad (6.2)$$

The term $[1 - \cos(kz_s \sin \theta(t_l))]$ contains the depth dependent harmonic content with an offset from the power calculation.

If the depth dependent interference is evenly sampled in time, a conventional Fourier transform could be used to relate the frequency content of the interference to source depth. However, because the harmonic is spaced evenly in $\sin \theta(t_l)$, McCargar and Zurk propose using a modified Fourier kernel to include the $\sin \theta(t_l)$ dependence [9],

$$M(z, w) = \int_c P(\omega, \alpha) e^{-i2kz\alpha} |d\alpha|, \quad \alpha = \sin \theta_{tr}(t_l), \quad (6.3)$$

where $P(\omega, \alpha)$ is the beamformed power output along the VTR trace. Applying the transform to the power from image theory in equation 6.2,

$$M(z, w) = 2 \frac{S^2(\omega)}{(\bar{z})^2} \int_{\alpha_1}^{\alpha_L} \alpha^2 e^{-i2kz\alpha} \left| \frac{d\alpha}{dt_l} \right| dt_l \otimes \frac{\pi}{k} [\delta(z) - \frac{1}{2} \delta(z \pm z_s)], \quad (6.4)$$

$$\alpha = \sin \theta_{tr}(t_l).$$

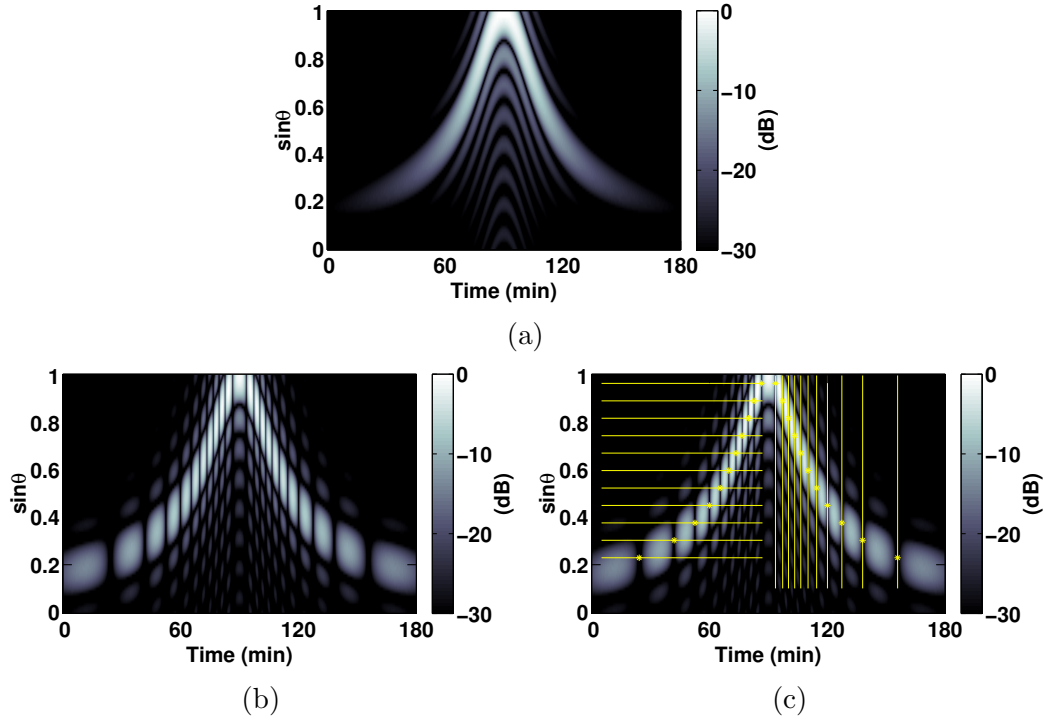


Figure 6.2: Depth based harmonic interference pattern from direct calculation of pressure through equation 6.1 followed by beamforming. Source is simulated moving on a constant speed trajectory, moving directly above a VLA at minute 90 of the 180 minute time span. (a) Simulated VTR for a source located 1 m below the surface showing low-frequency content in the $\sin \theta$ trajectory. (b) Simulated VTR for a source located 50 m below the surface exhibiting higher frequency content along the $\sin \theta$ trace. (c) VTR from (b) including spacing overlay indicating harmonic in $\sin \theta$.

The convolution, expressed by \otimes , indicates the result expected by image theory. The form of the expression in equation 6.4 with delta functions $\delta(z)$ and $\delta(z \pm z_s)$ predicts three peaks in the output, achieving depth separation. The $\delta(z)$ term indicates a zero peak associated with the power conversion in equation 6.2 and can be removed by proper demeaning. The peaks associated with $\delta(z \pm z_s)$ indicate a depth dependent result corresponding to the source depth. The $\delta(z)$ zero peak can be removed through demeaning. Demeaning is accomplished by subtracting half of the envelope from the

signal power trace in $\sin \theta(t_i)$. In this depth-based harmonic transform, frequency based filtering is not ideal because the low-frequency harmonic content is what defines sources near the surface. This envelope based demeaning method removes the residual low-frequency content from the beamformer power calculation without removing low-frequency harmonic content that may be caused by a surface source.

6.2 Simulated Harmonic Transform Results

A deep, 16-element, VLA is simulated with the source parameters in table 6.1 using the Ocean Acoustics Toolbox KRAKEN program [17]. A submerged target and a nearby surface interferer are simulated moving with constant velocities past the VLA with two different CPA times and ranges. Distant shipping interferers are also incorporated into the simulation. The receiver pressures are calculated over a 90 minute time span. Array elements are spaced every 3.75 *m* for a design frequency of 200 *Hz* and the mean array depth is 4920 *m*.

Parameter	Nearby Interferers	Distant Interferers	Submerged Target
# Sources	1	50	1
CPA Range (km)	7	>100	2
CPA Time (min)	10	-	65
Depth (m)	10	-	75
Speed (m/s)	13	-	5
Level (dB)	160	160	110

Table 6.1: Deep VLA simulation parameters for depth-based signal separation transform.

A flow diagram of the depth separation processing is shown in Figure 6.3 following

Depth Based Signal Separation Processing Flow

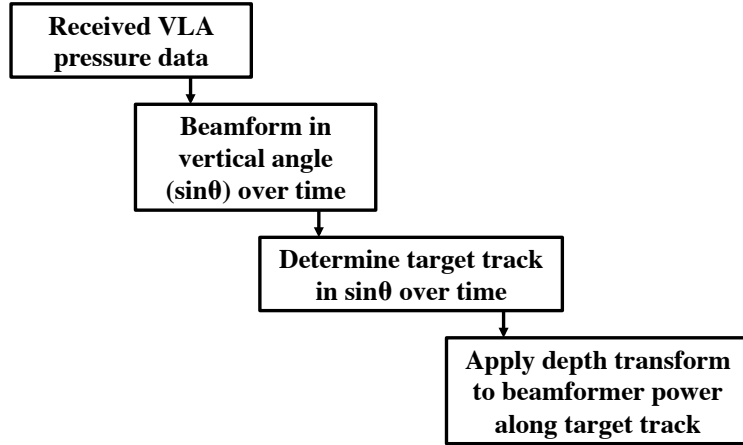


Figure 6.3: Diagram showing processing flow for depth-based signal separation as described by McCargar and Zurk [9].

the process outlined in McCargar and Zurk [9]. The received pressure signals are beamformed over the array and displayed on a VTR shown in Figure 6.4a. The $\sin\theta(t_i)$ traces are included in Figure 6.4b. The depth-based harmonic transform can be computed using the beamformer power output from the VTR traces as the input to equation 6.3. Prior to transforming the VTR trace, the data is demeaned to remove the $\delta(z)$ component from equation 6.4 and scaled in $\sin\theta(t_i)$ to normalize the received intensity as it decreases with range.

The transform outputs for the interferer and target traces are shown in Figures 6.4c and 6.4d respectively. Resolvable peaks for both the surface and submerged sources are visible in the transform outputs at least 5 *dB* above background. The peaks appropriately correspond with the simulated target and interferer depths. This is a

significant result, indicating the presence of two sources at different depths within the same viewable extent of a VTR without using any environmental information aside from the VLA element spacing and depth parameters. Using the transform as derived in accordance with the fields expected by image-theory, the successfully resolved peaks associated with targets at depth suggest that this method is robust to the influences of refraction within the RAP geometry.

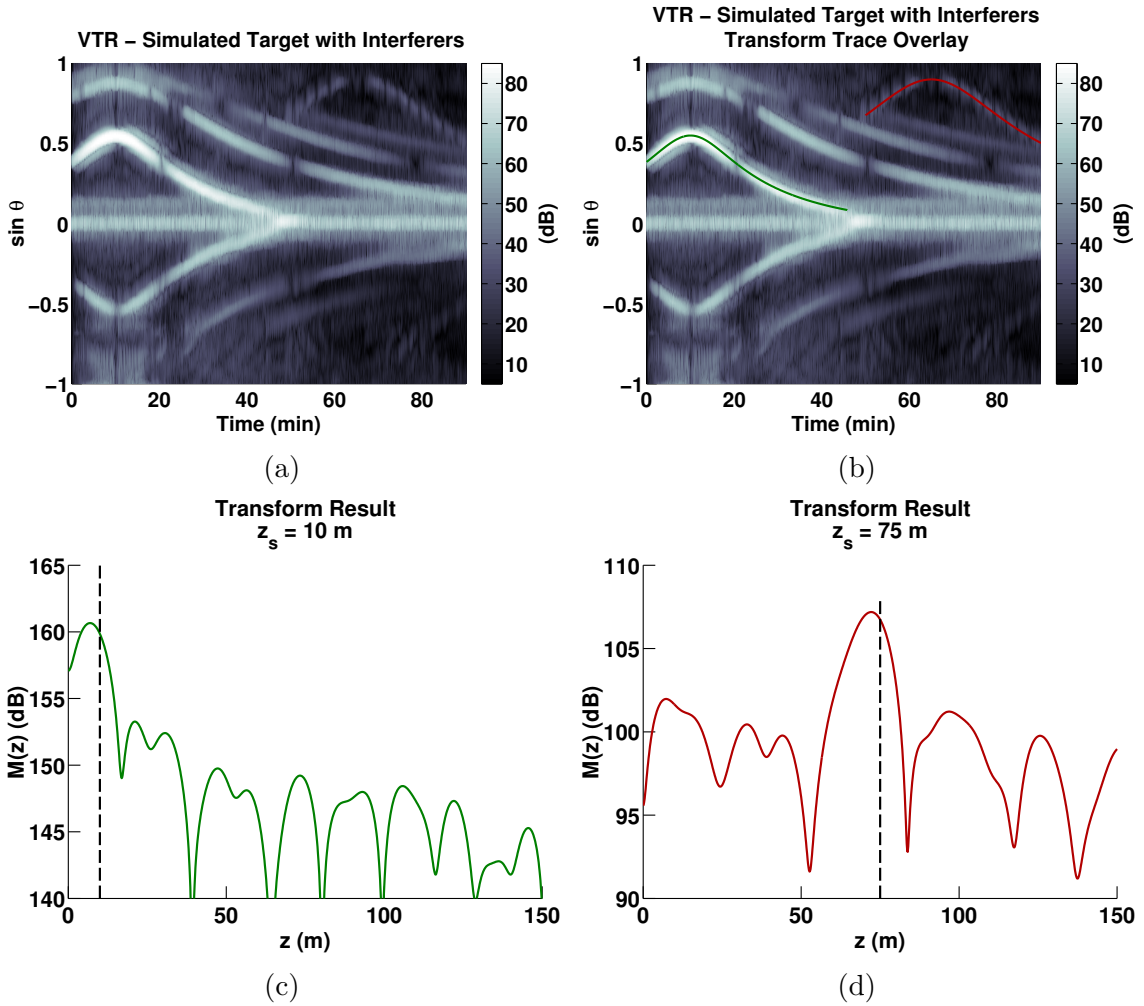


Figure 6.4: Simulated deep VLA VTR and depth-based signal separation transform results. (a) VTR plot showing target tracks in $\sin \theta$. (b) VTR with overlaid traces used for depth-based signal separation transform. (c) Transform result for surface interferer using green trace from (b) indicating source at 10 m depth. (d) Transform result for submerged target using red trace from (b) indicating source at 75 m depth.

As a source increases in depth, the $\sin \theta$ harmonic increases in frequency along the VTR track. When implementing a Fourier transform, there is a maximum resolvable frequency based on the sampling frequency of the time series data. Similarly, there is a limit to the resolvable depth given the resolution of the $\sin \theta$ track. By taking a

cut in $\sin \theta$, there is a coupling between the sampling in time and sampling in $\sin \theta$. In creating a VTR, data is segmented and a beamformer output is computed for each snapshot in time at a given frequency. Assuming continuous sampling in $\sin \theta$ by beamforming for all $\sin \theta$ values on the hypothesized VTR track, the maximum resolvable depth can be calculated from the minimum sampling frequency in $\sin \theta(t_l)$ by,

$$z_{Nyquist} = \frac{1}{2} \frac{\pi c}{\omega_o} \min \left(\frac{1}{\frac{\Delta \sin \theta(t_l)}{\Delta t}} \right). \quad (6.5)$$

The term $\frac{\pi c}{\omega_o}$ is equal to $\frac{\pi}{k}$, where k and ω_o are the wavenumber and the radial frequency used in beamforming to create the VTR, respectively. This result achieves a resolvable depth limit based solely on the time resolution of the VTR.

This depth limit can be used to select proper snapshot intervals in creating the VTR used to resolve the harmonic present in the target track. Producing a VTR with time snapshots based on a desired frequency resolution may not provide ideal sampling once a target track in $\sin \theta$ is selected. Based on a hypothesized target track, equation 6.5 can be reformulated to calculate the required linear resolution in time Δt , which corresponds to snapshot length, to resolve harmonics in the VTR track up to a desired depth,

$$\Delta t = \frac{1}{2} \frac{\pi c}{z_{Nyquist} \omega_o} \max (\Delta \sin \theta(t_l)). \quad (6.6)$$

Using the simulated tracks shown in the VTR in Figure 6.4b, unambiguous depth limits are calculated using equation 6.5 for differing snapshot lengths and displayed in

Table 6.2. The simulated transform results were calculated using a snapshot length of 2.5 *s* which yields an unambiguous depth of approximately 2 *km* for both the submerged target and surface interferer tracks. This is not a reasonable depth limit given that other parameters influence the presence of depth-based harmonic content for deep sources along a VTR track. The depth-based separation technique presented by McCargar and Zurk relies on the inability of a beamformer to spatially resolve the arrivals from source and surface reflection, thereby creating an interference pattern along a single track. In application, with increased depth, the angular separation of a source from the image increases. The interference along a VTR track is removed when beamforming can successfully resolve the arrivals [26].

Unambiguous Depth

Snapshot Length (s)	Simulation Track	
	Surface Interferer	Submerged Target
2.5	2.0 <i>km</i>	2.2 <i>km</i>
5	1.0 <i>km</i>	1.1 <i>km</i>
7.5	680 <i>m</i>	740 <i>m</i>
10	510 <i>m</i>	560 <i>m</i>
12.5	410 <i>m</i>	440 <i>m</i>

Table 6.2: Calculated unambiguous depth limits based on VTR tracks from Figure 6.4 using equation 6.5.

In passive applications, longer snapshots accumulate signal power and are desirable when trying to identify weak signals. Increasing the snapshot length to 10 *s*

reduces the sampling frequency of the VTR track in $\sin \theta$ and limits the unambiguous depth to approximately 500 *m*. Further increasing snapshot length continuously decreases the maximum unambiguous depth.

This derived depth limit based on sampling in time provides an expected unambiguous depth. The ability to successfully resolve submerged targets near the surface can enhance tracking of traces in $\sin \theta$ by adding a hypothesis for the expected harmonic fluctuations. For tracks approaching array broadside where $\sin \theta$ is small, the differential range to the VLA decreases, making the harmonic vary slowly in time. The beating pattern in Figure 6.2c shows small variations near broadside where the beating pattern spreads in time. This can become difficult to track as the fluctuations are slow and reducing in intensity with increased range.

Chapter 7

Summary and Future Work

7.1 Summary

The presence of time-frequency interference structure is ubiquitous in received sonar data for active and passive systems. In many cases, parameters influencing the multipath interference structure such as bathymetry and sound speed profile are not exactly known and are therefore not reliable resources for mitigating effects on received data. Methods for utilizing the presence of interference in sonar array data were presented, enhancing the target localization abilities of more conventional processes.

A proposed method for extracting interference structures present in spectrograms was applied to simulated active HLA data in Chapter 5. This method was based on previously proposed usage of the Radon transform with the additional processing of Fourier transformation of the projected result to extract the spacing of interference striations. This method was also successfully applied to simulated deep VLA data exhibiting multiple striation patterns in a single phone-frequency spectrogram in Section 5.3. The proposed method aids in the visual examination of spectrogram striations by composing a distribution of slopes supplemented with striation spacing.

The method of striation-based beamforming derived by Zurk and Rouseff [7, 8] was applied to interference striations in broadband outputs for simulated HLA and

VLA data. In both of these applications, the striation patterns are easily visible. In the case of the simulated HLA presented in this thesis, striations were clearly visible. Cuts through the maximal bearing were used to show the progression of preserved striations in the beamformed output with changing target range. The presence of multiple striation patterns within a single spectrogram, as seen in the simulated VLA data, prove more difficult to determine through visual examination. The simulated VLA result provided an example of a geometry where conventional single-frequency beamforming preserved one set of striations. The further processing of striation-based beamforming was shown to preserve the structure of a second set of striations, using the slope determined by the Radon and Fourier transform based extraction method.

In Chapter 6, the method of depth-based signal separation described by McCargar and Zurk [9] proved successful in separating surface sources from submerged sources using simulated signals received at a deep VLA. Successful separation of simulated near surface sources in depth using the Ocean Acoustics Toolbox KRAKEN program [17] suggests that the image-theory derived transform is robust to arrivals influenced by refraction through the RAP geometry. An expression for the maximum resolvable depth was presented for use with the depth separation transform. The resolvable depth limit was derived based on the time sampling used to compute the beamformed output creating the VTR used to determine a target track.

7.2 Future Work

The application of striation-based beamforming to experimentally acquired data has been limited. In the work of Zurk and Rouseff [7, 8], in which striation patterns are easily visible, the striation-based beamforming method successfully preserves the interference structure. In the presence of noise and multiple sources of interference striations, successful implementation of striation beamforming will be reliant on the ability to extract layers of spectrogram striations from a single image and sufficient bandwidth to resolve the slope of the striation. In future work, the striation extraction method and striation-based beamforming can be used in processing experimental data in differing geometries. The time-frequency arrival structure over vertical apertures can also be explored. Due to the computational requirements of normal mode broadband array simulation, mid-frequency and high-frequency simulations were not included in the scope of this thesis. Additional simulation at higher frequencies will give more insight into waveguide invariant phenomena when applied to active sonar.

The depth dependent harmonic has been largely explored in relation to noise and separation of two resolvable tracks on a VTR. Continued research into the presence of harmonic content for deeper sources and tracks that provide limited range in vertical angle can further characterize the ability of the proposed transform in McCargar and Zurk to resolve targets in range and depth. Additionally, application of this method to experimental data is largely limited due to the associated costs, technical

requirements, and restricted distribution of aquired data.

References

- [1] S. D. Chuprov, Interference structure of a sound field in a layered ocean, in *Ocean Acoustics: Current State*, edited by L. M. Brekhovskikh and I. B. Andreevoi, Nauka, Moscow, (1982)
- [2] L. M. Brekhovskikh and Y. P. Lysanov, *Fundamentals of Ocean Acoustics*, 3rd ed., Springer, NY, (2002)
- [3] L. M. Zurk, H. Ou, and R.L. Campbell Jr., Effect of the target scattering function on active waveguide invariance striations, *Proc. IEEE Oceans*, Seattle, WA, (2010)
- [4] L. M. Zurk, D. Rouseff, J.E. Quijano and G. Greenwood, Bistatic invariance principle for active sonar geometries, *Proc. Eighth European Conference on Underwater Acoustics*, Carvoeiro, Portugal, 787-791, (2006)
- [5] J. E. Quijano, R.L. Campbell Jr., T.G. Oesterlein, and L.M. Zurk, Experimental observations of active invariance striations in a tank environment, *J. Acoust. Soc. Am.*, **128**(2), (2010)

- [6] D. Rouseff and R. C. Spindel, Modeling the waveguide invariant as a distribution, in *Ocean Acoustic Interference Phenomena and Signal Processing*, edited by W.A. Kuperman and G.L. D'Spain, *AIP Conf. Proc.*, 621, 137-148, (2001)
- [7] L. M. Zurk and D. Rouseff, Striation-based beamforming for active sonar with a horizontal line array, *J. Acoust. Soc. Am.*, **132**(4), EL264, (2012)
- [8] D. Rouseff and L. M. Zurk, Striation-based beamforming for estimating the waveguide invariant with passive sonar, *J. Acoust. Soc. Am.*, **130**(2), EL76, (2011)
- [9] R. McCargar and L. M. Zurk, Depth-based signal separation with vertical line arrays in the deep ocean, *J. Acoust. Soc. Am.*, 133, EL320, (2013)
- [10] M. B. Porter and Y. Liu, Finite-Element Ray Tracing, *Theoretical and Computational Acoustics - Volume 2*, edited by D. Lee and M. H. Schultz, World Scientific, (1994)
- [11] R. Gaul, D. Knobles, J. Shooter, and A. Wittenborn, Ambient noise analysis of deep ocean measurements in the northeast pacific, *IEEE J. Ocean Eng.*, **32**, 497-512, (2007)
- [12] Z. Li, "Vertical Noise Structure and Target Detection Performance in Deep Ocean Environments", Portland, OR, Portland State University, (2010)

- [13] Z. Li, L. M. Zurk, and B. Ma, Vertical arrival structure of shipping noise in deep water channels, *Proc. IEEE Oceans*, Seattle, WA, 1-8, (2010)
- [14] F. B. Jensen, W. A. Kuperman M. B. Porter, and H. Schnidt, *Computational Ocean Acoustics*, AIP, New York, (1994)
- [15] L.E. Kinsler, A.R. Frey, A.B. Coppens, and J.V. Sanders, *Fundamentals of Acoustics*, Wiley, New York, (2000)
- [16] A. Huyer, Coastal upwelling in the California current system, *Progress in Oceanography*, **12**(3), 259-284, (1983)
- [17] M. B. Porter, The KRAKEN normal mode program, *Technical Report, DTIC Document*, (1992)
- [18] W. A. Kuperman and J. F. Lynch, Shallow-Water Acoustics, *Physics Today, Am. Inst. of Physics*, 55-61, (2004)
- [19] W. H. Munk, Sound channel in an exponentially stratified ocean with applications to SOFAR, *J. Acoust. Soc. Am.*, **66**, 250-255, (1979)
- [20] C. He, “Enhanced Kalman Tracking Algorithm Using the Invariance Principle and the Multi-Frequency Tracking Algorithm”, Portland, OR, Portland State University, (2008)
- [21] C. He, J. E. Quijano, L. M. Zurk, Enhanced Kalman Filter Algorithm Using the Invariance Principle, *IEEE J. Oceanic Eng.*, 34(4), 575-585, (2009)

- [22] L. M. Zurk, Passive detection in deep water using the reliable acoustic path, *J. Acoust. Soc. Am.*, **125**, 2576 (2009)
- [23] L. Emery, M. Bradley, and T. Hall, Data Base Description (DBD) for the Historical Temporal Shipping Data Base (HITS), Version 4.0, *PSI Technical Report TRS-301*, (2001)
- [24] J. E. Quijano, L. M. Zurk, and D. Rouseff, Demonstration of the invariance principle for active sonar, *J. Acoust. Soc. Am.*, **123**, 1329-1337, (2008)
- [25] F. Ingenito, Scattering from an object in a stratified medium, *J. Acoust. Soc. Am.*, **82**, 2051-2059, (1987)
- [26] H. Van Trees, *Optimum array processing*, volume 7, Wiley, New York, (2002)
- [27] J. Canny, A computational approach for edge detection, *IEEE Trans. Pattern Anal. Machine Intell.*, **8**(6), 679-698, (1986)
- [28] R. Gonzalez and R. Woods, *Digital Image Processing*, Springer, New York (2011)
- [29] K.L. Cockrell and H. Schmidt, Robust passive range estimation using the waveguide invariant, *J. Acoust. Soc. Am.*, **127**(5), 2780-2789, (2010)